Annexure – B
Salient Research Achievements

Contents

PART-I: MIXED PIXEL ANALYSIS

The general method of analyzing mixed pixel spectral response is to decompose the actual spectra into several pure spectral components representing the signatures of the endmembers. The present work suggests a reverse engineering of standardizing the mixed pixel spectrum for a certain spatial distribution of endmembers by synthesizing spectral signatures with varying proportions of standard spectral library data and matching them with the experimentally obtained mixed pixel signature. The idea is demonstrated with hyperspectral UV-vis-NIR reflectance measurements on laboratory generated model mixed pixels consisting of different endmember surfaces, *viz.* concrete, soil, brick and vegetation and hyperspectral signatures derived from Hyperion satellite images consisting of concrete, soil and vegetation in different proportions. The experimental reflectance values were compared with computationally generated spectral variations assuming linear mixing of pure spectral signatures. Good matching in the nature of spectral variation was obtained in most cases. The present concept hopes that hyperspectral signatures of mixed pixels can be synthesized from the available spectral libraries and be matched with that obtained from satellite images even with less number of bands. Thus enhancing the computational job in laboratory can moderate the keen requirement of high accuracy of remote sensor and band resolution thereby reducing data volume and transmission bandwidth.

1.1. Introduction

Hyperspectral sensing, *i.e.* remote sensing and imaging in hundreds of contiguous narrow spectral bands can detect, discriminate and classify many subtle features of ground objects. The obvious advantage over the conventional multiband sensing is higher spectral discrimination of reflectance that has made hyperspectral sensing popular to precision agriculture (Zarco-Tejada *et al.* 2005), vegetation canopy modeling (Panferov *et al.* 2001), vegetation species identification (Alberotanza *et al.* 1999), mineral exploration (Howari *et al.* 2002), snow measurements (Nolin and Dozier 2000), coastal analysis (Brando and Dekker 2003), environmental studies (Salem *et al.* 2005), target

detection (Kwon and Nasrabadi 2005), military appliances (Moorhead *et al.* 2001) and many other applications.

Hyperspectral imaging is not a mere extension to the conventional multiband processes with the number of bands enhanced. It emphasizes on the spectral domain and calls for new approaches in the analysis techniques as may found in literature (Varshney and Arora 2004, Chang 2007). One of the subjects of interest in hyperspectral remote sensing is the spectral analysis of mixed pixels, when several small size targets get embedded in a single imagery pixel, each one contributing to the resultant spectral reflectance of that pixel. A popular method of analyzing such hyperspectral data is linear mixing (Mazer *et al.* 1988, Settle 1996, Manolakis *et al.* 2001), which assumes the measured spectra as linear superposition of several pure spectra produced by different targets present in small spatial extent. For multiple scattering of radiation between elements in the scene, nonlinear mixing occurs (Borel and Gerstl 1994).

Whatever may be the process of analysis, the general approach is to somehow decompose the experimentally obtained hyperspectral data into a number of pure spectra of the constituent materials applying various computational techniques on the DN values. The determination of the endmember spectra is based solely on the information contained within the image. Therefore, the satellite sensor for image acquisition must be of the best possible spectral resolution and reflectance quality thereby increasing data volume and redundancy due to correlation between adjacent spectral channels.

The present work suggests a reverse engineering of synthesizing hyperspectral signatures with standard library data for different proportions of endmembers and comparing them with the experimentally obtained mixed pixel signatures. The best match should be considered as the actual condition of endmember distribution in the pixel. The idea is demonstrated with different proportions of reflectance data on both laboratory-measured objects and endmembers selected from satellite images. The experimental reflectance values are compared with computationally generated spectral signatures using linear mixing of previously known spectral signatures and good matching is obtained in the nature of spectral variation. Thus the present work proposes a new model for spectral matching with synthesized spectra demonstrated with simple linear mixing of some common objects. It requires more computational developments as further scope for study.

In fact, that is the claimed merit of this technique because precise spectral libraries are available on different varieties of pure endmembers. Spectral synthesis by random selection, matching with the signature obtained from satellite image and conclusion on the relative weight of endmembers are the workloads shared by the computer. Enhancing the computational job in laboratory can moderate the keen requirement of high accuracy of remote sensor and band resolution.

1.2. Methodology

The work comprises reflectance measurement in laboratory for a few sample objects and sampling of endmembers from satellite images. In one phase of the work, model mixed pixels and their hyperspectral signatures were generated in laboratory involving natural and man-made objects, namely loam type soil (33–35% moisture), vegetation, brick and concrete. Fresh banana leaves were made to serve the purpose of vegetation. The hyperspectral reflectance for each object was measured throughout the UV-vis-NIR region (300-1000 nm) with 1 nm resolution with ASD FieldSpec spectroradiometer having angular field of view (FOV) fixed at 25°. The reflectance values were calibrated with Spectralon white reference panel acting as Lambertian surface and the measurements were carried out in open sunshine near solar noon. The sensor was held vertically downward 1 m above the surface so that the ground FOV was a circular area of approximately 22 cm radius, simulating a single pixel. The characteristic reflectance-wavelength variation for such a pixel of each object was obtained separately as shown in Figure 1(a). The surface area of each object under the FOV was partly covered with fresh banana leaves, as indicated in Figure 1(b), to simulate partial vegetation cover of different extent for each object. Thus the signatures for the mixtures of two different endmembers, namely concrete-vegetation, brick-vegetation and soil-vegetation were generated at different proportions as shown in Figure 2(a) through 2(c).

As an extension of the above work, 50 cm × 50 cm square surface areas of four endmembers, namely concrete, brick, loam soil (33–35% moisture) and vegetation were tiled together. The spectroradiometer sensor was held vertically downward at a height of 2 m just above the junction point (P) of the four different surfaces, as indicated in figure

2(d) so that it could find a mixed pixel of circular area of approximately 44 cm radius comprising equal proportions of four endmembers. Figure 2(d) shows the resultant reflectance-wavelength plots obtained for different proportions of these four endmembers.

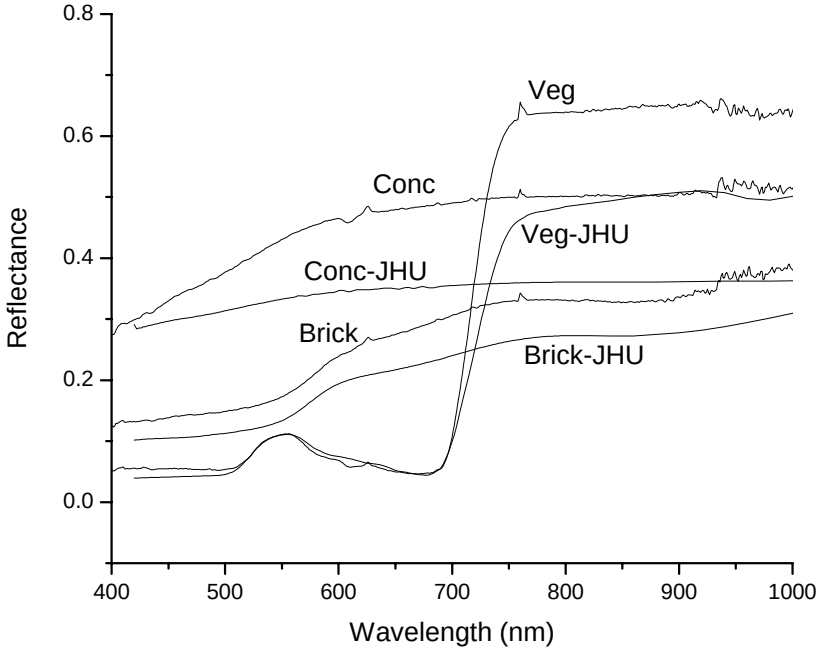

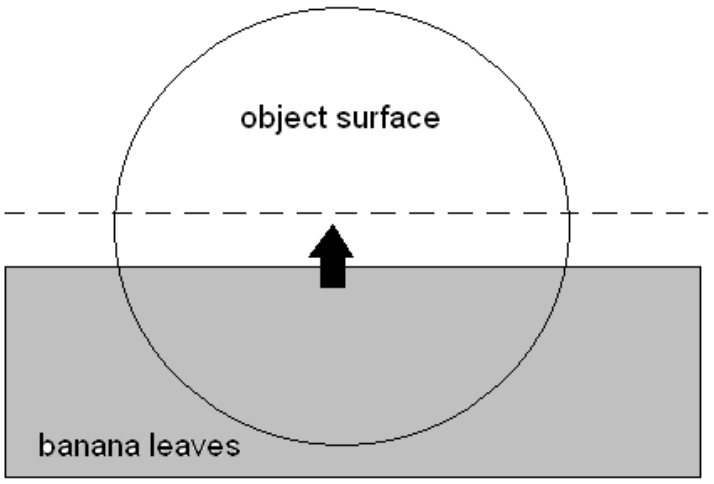

Figure 1: (a) Comparison of present experimental reflectance-wavelength plots for concrete (Conc), brick (Brick) and vegetation (Veg) with those obtained from the spectral library of John Hopkins University (JHU) (b) layout of simulating partial vegetation cover

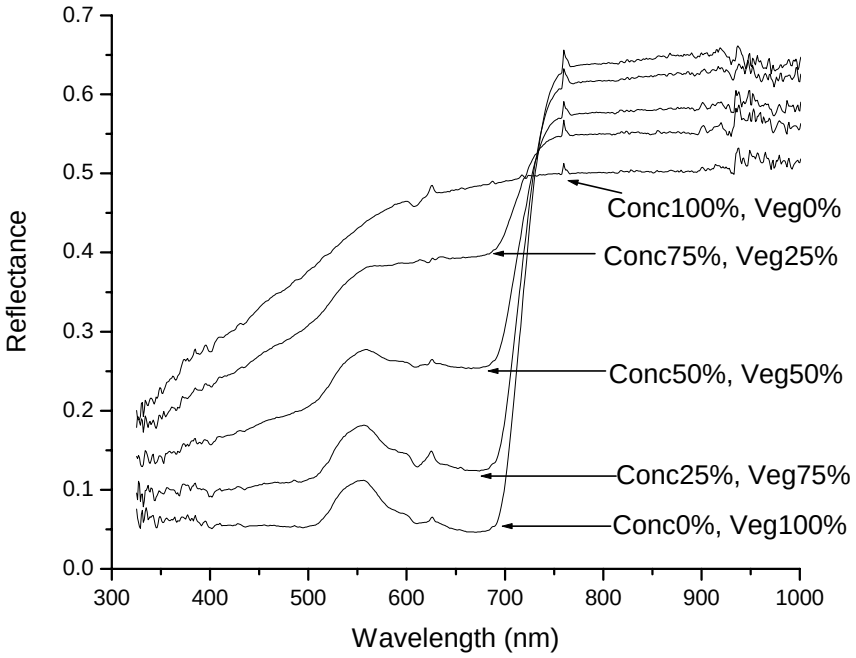

(a)

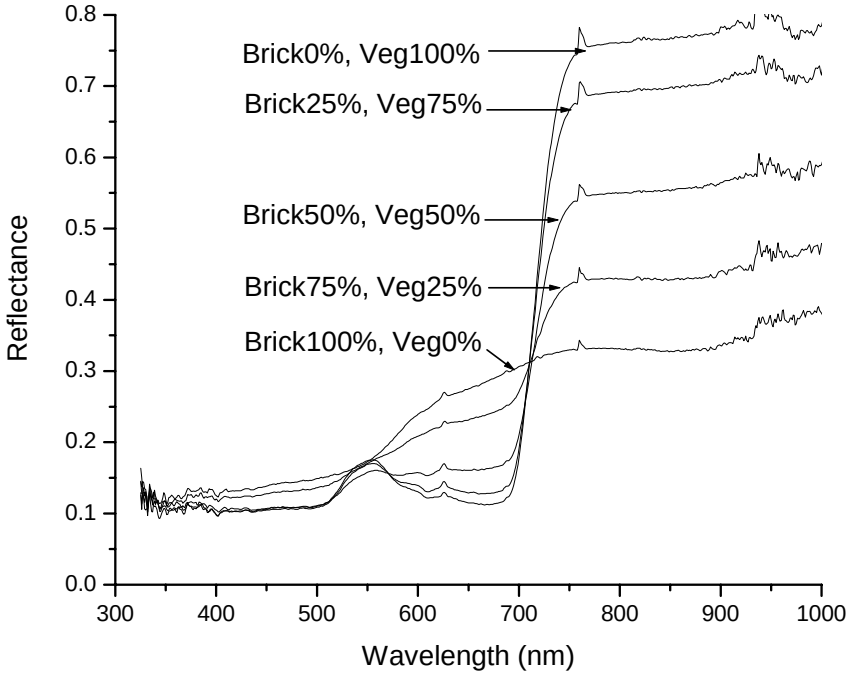

(b)

Figure 2: Experimental reflectance-wavelength plots obtained with the mixtures of different endmembers under the FOV: (a) concrete and vegetation, (b) brick and vegetation, (c) soil and vegetation and (d) these four objects tiled in different proportions, as indicated. The pure pixels are indicated by '100%' and different proportions of their mixtures are indicated against the curves.

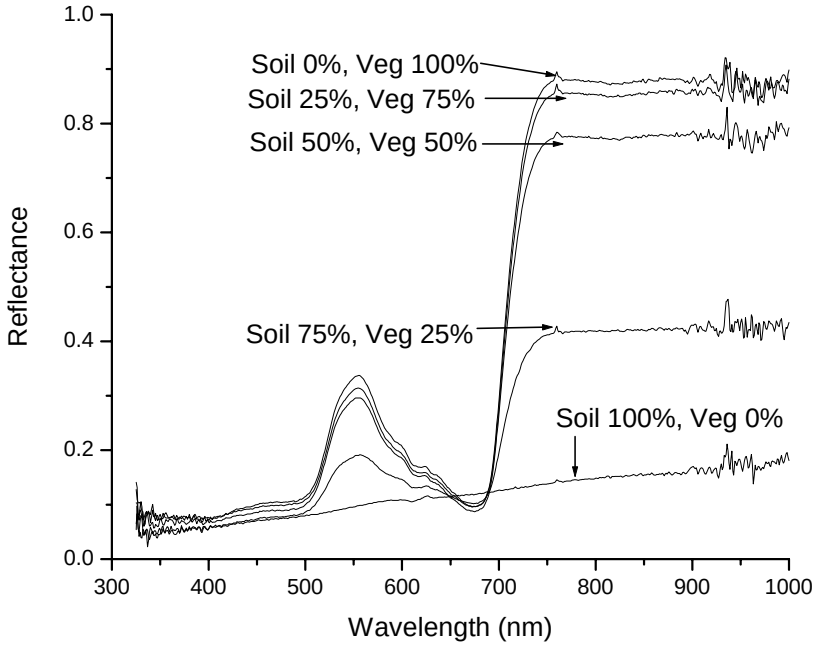

(c)

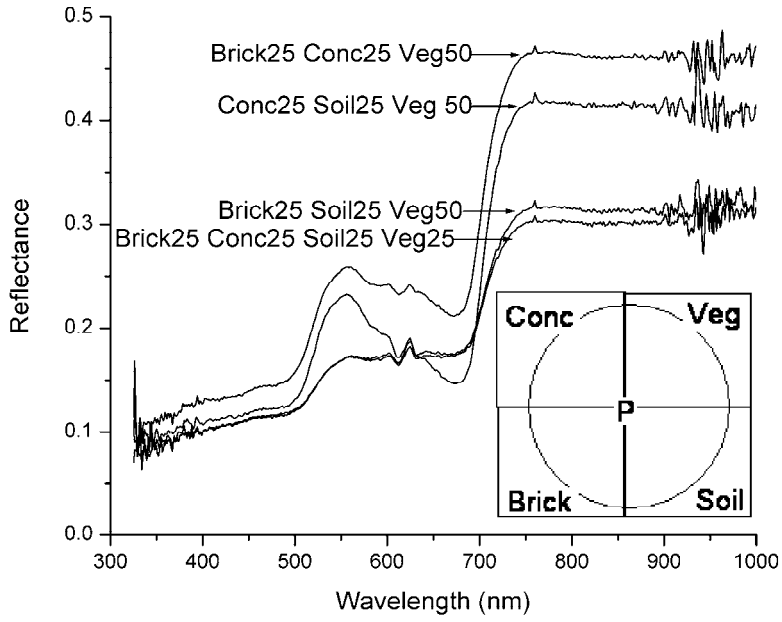

(d)

Figure 2: Experimental reflectance-wavelength plots obtained with the mixtures of different endmembers under the FOV: (a) concrete and vegetation, (b) brick and vegetation, (c) soil and vegetation and (d) these four objects tiled in different proportions, as indicated. The pure pixels are indicated by '100%' and different proportions of their mixtures are indicated against the curves.

Solar irradiance spectrum was measured at 1 nm resolution throughout the same UV-Vis-NIR range with the same ASD instrument fitted with remote cosine receptor on the 25º FOV fiber and kept facing vertically upward irrespective of the solar elevation. Data were collected at different seasons and different atmospheric conditions placing the instrument at the same place and height of open air. Some of the irradiance data have been used as reference later.

In the other phase of the work, satellite images of different spatial and spectral resolutions were analyzed using ENVI 4.5 image processing software. Multispectral image procured by Ocean Color Monitor (OCM) sensor (ground resolution 360×236 m) of Indian Remote Sensing Satellite IRS-P4 for a region around Chilika Lagoon (85º15´E–85º30´E and 19º30´N–19º45´N) of eastern coast of India was analyzed. The pure endmember regions were selected by Minimum Noise Fraction (MNF) transform and Pixel Purity Index (PPI) techniques, the software having built-in facilities for these analysis techniques.

Table 1. Specifications of sensor OCM of satellite IRS-P4. Ground resolution 360×236 m (Mishra *et al.* 2008)

Bands	Wavelength Range (nm)	Central Wavelength (nm)
Band-1	404–424	414.2
Band-2	432–452	441.4
Band-3	479–499	485.7
Band-4	502–522	510.6
Band-5	547–567	556.4
Band-6	660–680	669.0
Band-7	748–788	768.6
Band-8	847–887	865.1

The OCM consists of only eight bands within visible and NIR regions, as mentioned in Table-1. To illustrate the spectral signature more accurately, Hyperion hyperspectral images (ground resolution 30 m) for Kolkata city and nearby area (centred

around 22°35′ N, 88°24′ E) were downloaded from USGS website. The digital number (DN) values were converted to reflectance (R) for fifty VNIR waveband channels (No. 8 to 57) using the formula

$$R = \frac{\pi L_\lambda d^2}{ESUN_\lambda \cos\theta} \tag{1}$$

where

L_λ = DN/40 is the radiance ($Wm^{-2}sr^{-1}\mu m^{-1}$) as function of wavelength

d = earth-sun distance in astronomical units

$ESUN_\lambda$ = hyperion mean solar exoatmospheric irradiance ($Wm^{-2}\mu m^{-1}$) as function of wavelength and

θ = solar zenith angle

1.3. Results and Discussion

Figure 1(a) compares the present experimental reflectance-wavelength plots for concrete (Conc), brick (Brick) and fresh banana leaf (Veg) with standard signatures of concrete (Conc-JHU), brick (Brick-JHU) and green grass (Veg-JHU), respectively, obtained from the spectral library of John Hopkins University (JHU).

Figure 2 represents the experimental reflectance-wavelength plots obtained with the mixtures of different endmembers under the FOV: (a) concrete and vegetation, (b) brick and vegetation, (c) soil and vegetation and (d) these four objects in different proportions. The pure pixels are indicated by '100%' and different proportions of their mixtures are indicated against the curves. The general trend of the resultant signature of the region under the FOV is found to approach that of vegetation as the vegetation-covered portion increases.

Such mixed pixel signatures with different endmembers were also computationally generated with the assumption of linear mixing using the individual experimental spectra of pure endmembers. The general algorithm presented in figure 3 was used to compute data for the mixed spectra for different combinations of two and four endmembers. The results are illustrated in figures 4(a) through 4(d) and may be compared with the experimental results of figures 2(a) through 2(d), respectively.

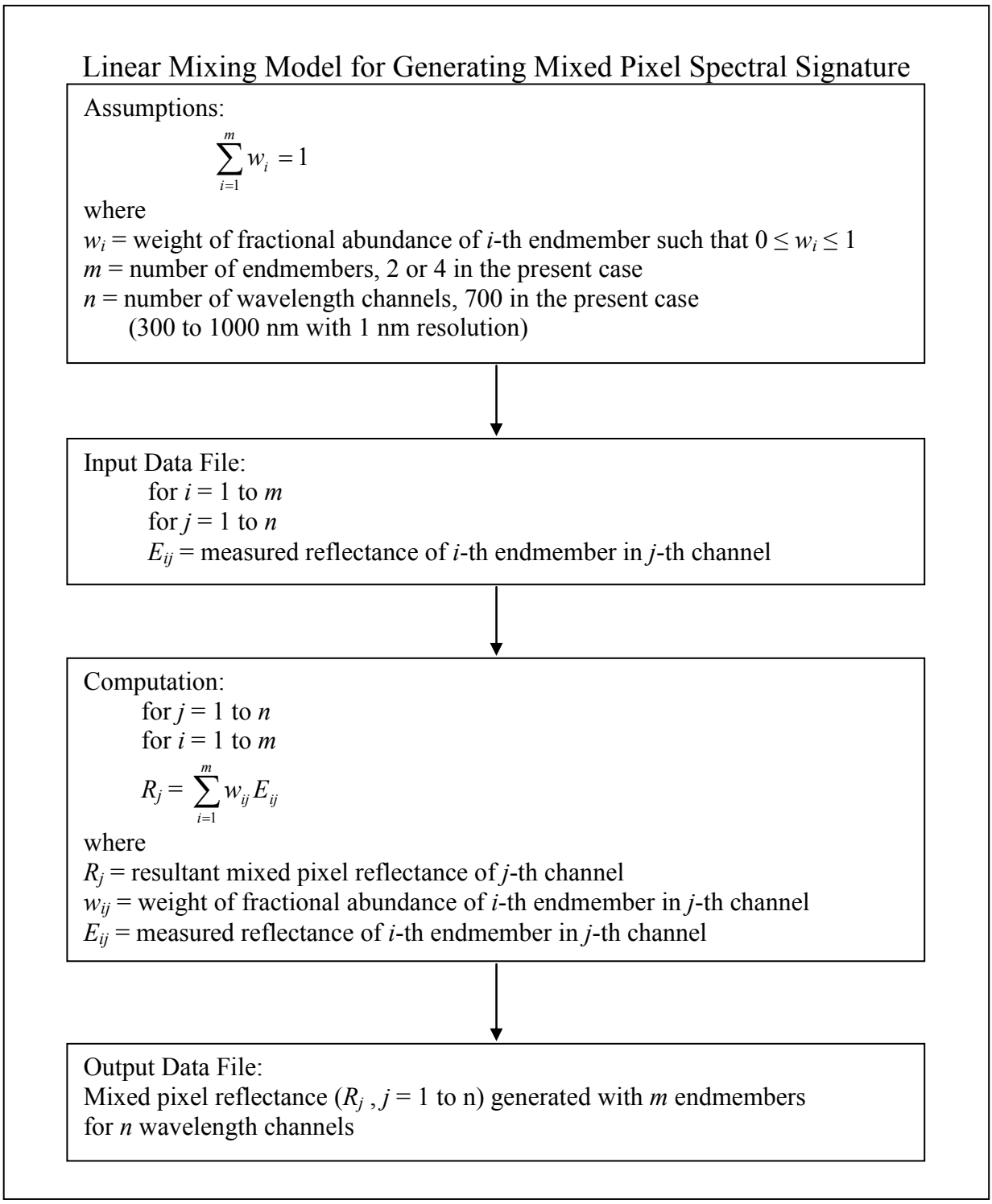

Figure 3: General algorithm for computationally generating mixed pixel spectra for different possible linear combinations of endmembers using their experimentally obtained individual spectral data.

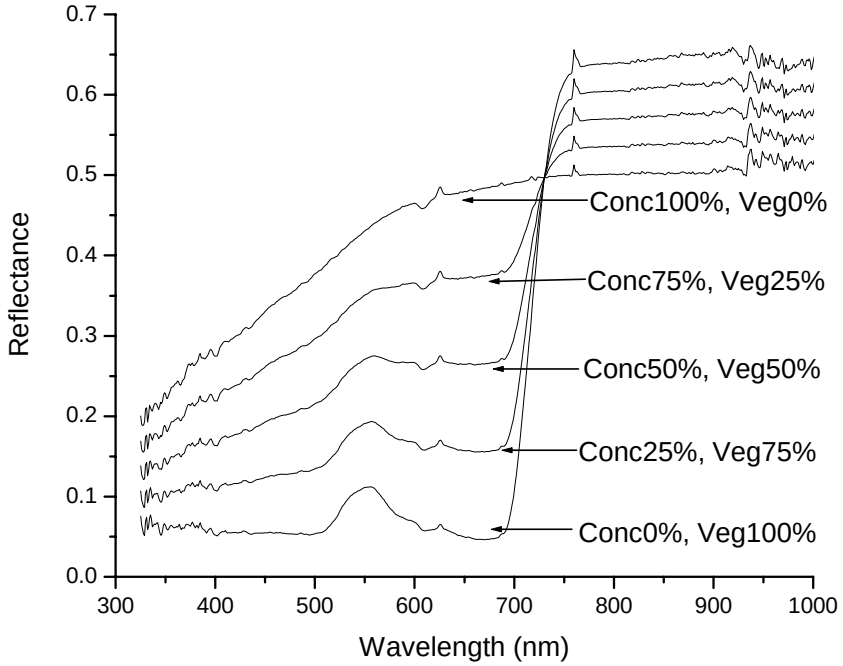

(a)

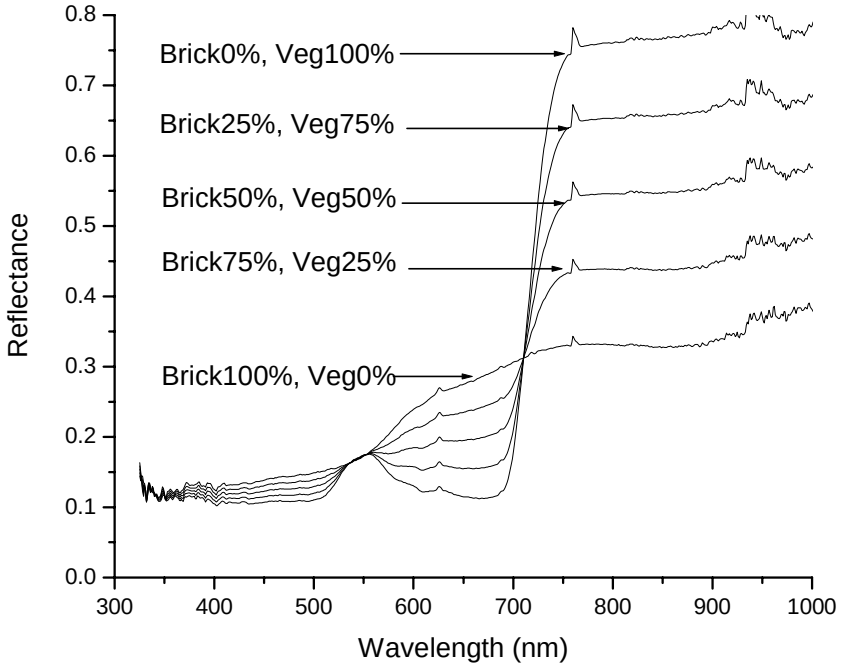

(b)

Figure 4: Computationally synthesized reflectance-wavelength plots for mixed pixels with different proportions of endmembers: (a) concrete and vegetation, (b) brick and vegetation, (c) soil and vegetation and (d) different proportions of these four, simulated by linear mixing of their individual experimental spectra.

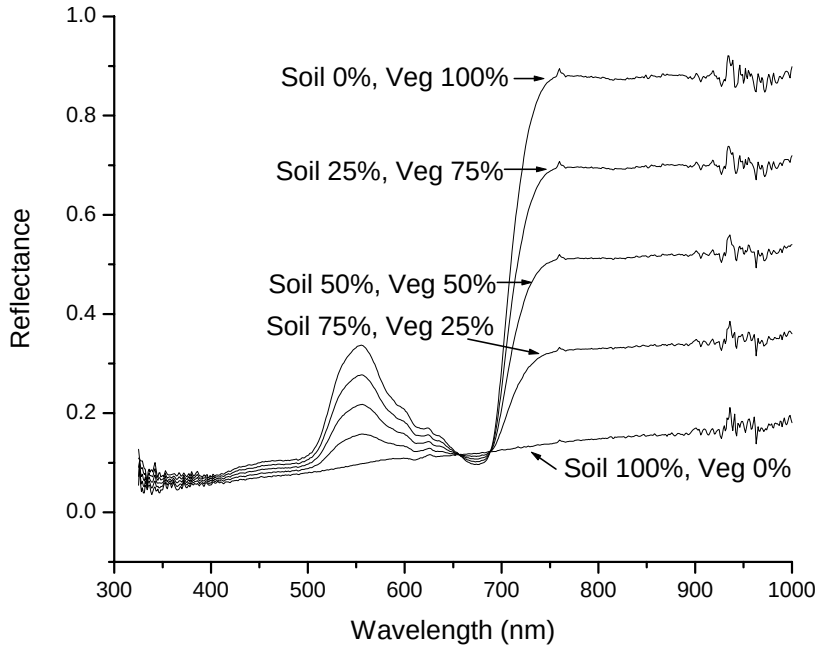

(c)

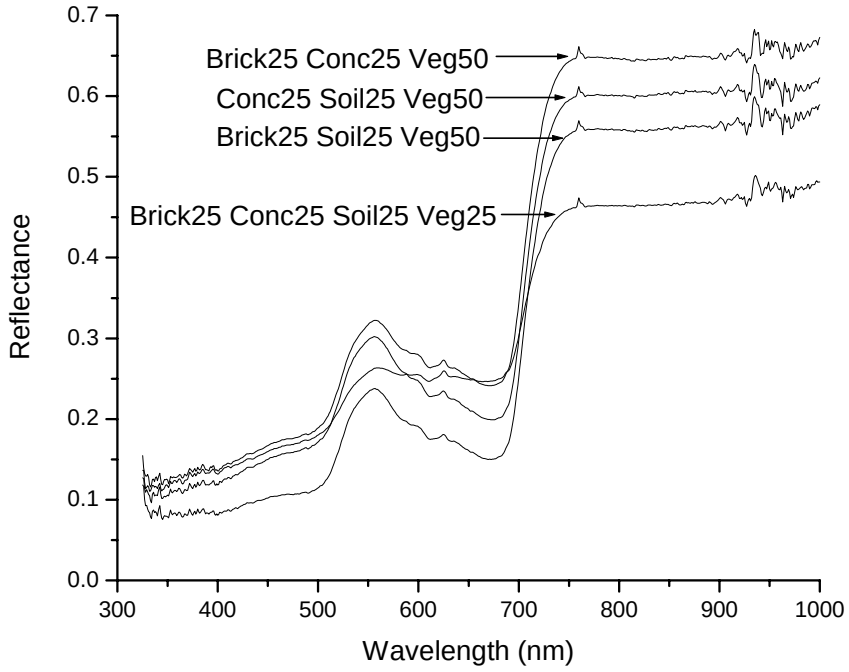

(d)

Figure 4: Computationally synthesized reflectance-wavelength plots for mixed pixels with different proportions of endmembers: (a) concrete and vegetation, (b) brick and vegetation, (c) soil and vegetation and (d) different proportions of these four, simulated by linear mixing of their individual experimental spectra.

Good agreement is obtained in most cases on comparing the original spectra with those simulated with linear mixing of the individual spectra. Thus, it possible to synthesize the mixed pixel spectra and to predict the relative weight of different endmembers in a mixed pixel spectrum provided that the spectra of the individual members are properly selected from the library.

The next part of the work is the comparison of the spectral signature (wavelength-reflectance plot) extracted from the satellite image with that established by spectroradiometry in laboratory as above. Let us start with vegetation signature because it has a typical nature and it is easily obtained in pure pixel form in the images.

Figure 5(a) shows a portion of the OCM image consisting of Chilika Lagoon(A), deep sea of Bay of Bengal(B), vegetation/ forest(C) and bare/ cultivated soil(D) sorted out by MNF transform and identified by Google Earth imaging. The average normalized DN values for vegetation (C) and soil (D) zones were calculated for the eight available wavebands and their fractional combinations were generated by linear summation as plotted in figure 5(b). No definite result is apparent from the graph. However, careful observation reveals a regular change with the vegetation-soil ratio, especially at the red-NIR transition region.

With a hope for more accurate reflectance variation with wavelength, vegetation spectral signatures were derived from Hyperion hyperspectral satellite images. These are shown in figure 6(a) [rainy season: July 27, 2002] and figure 6(b) [winter season: January 6, 2010]. Obviously there is also a wide span of time between these two. A famous river named Ganga is visible there making it convenient to locate the city. The spectral signatures of vegetation were derived from a number of randomly chosen pure pixel vegetated zones. Such regions are denoted by ‘A’ in figures 6(a) and 6(b). A few such vegetation spectra derived from some randomly chosen zones of figure 6(a) are shown in figure 7(a). The different pure vegetated zones yielded almost the same spectral variation. Apparently these are looking quite different from the spectral variations obtained in laboratory. The reason is the absorptions due to oxygen (around 760 nm) and water vapour (around 810 & 900 nm). Figure 7(b) further clarifies it. The water vapour absorption is much reduced in winter as noted from the vegetation spectral signature obtained from figure 6(b).

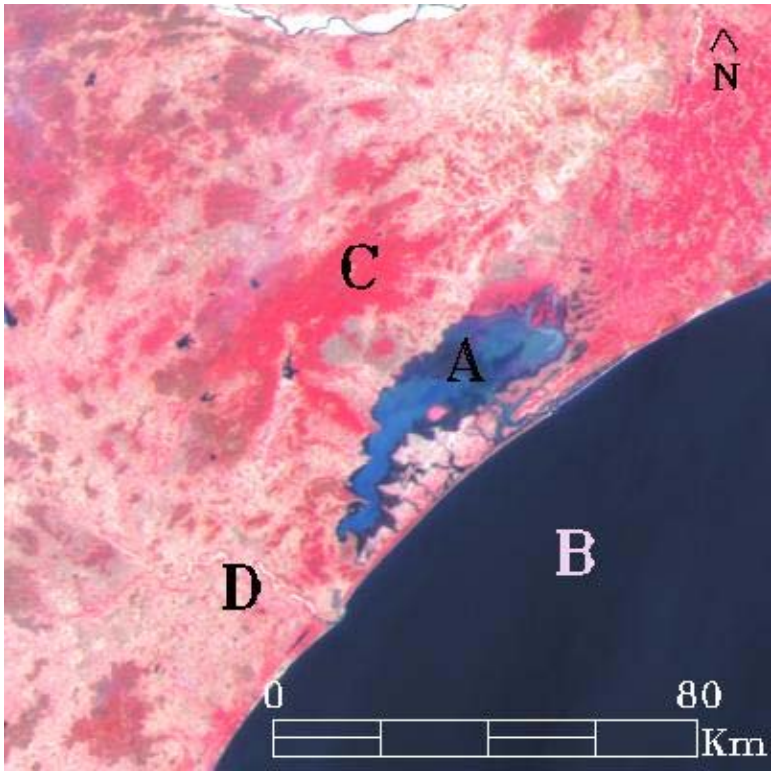

(a)

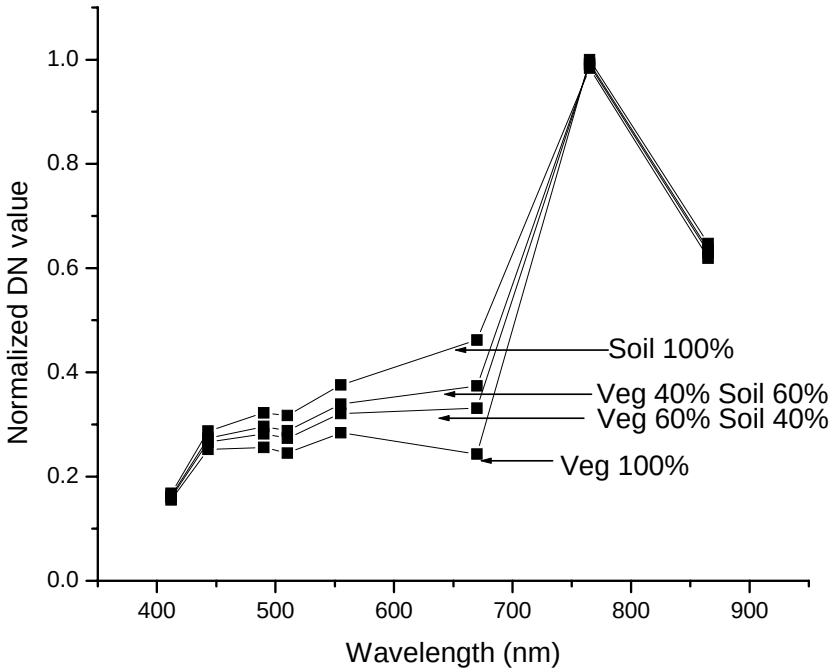

(b)

Figure 5: (a) IRS P4 OCM image composed of bands 5, 6 and 7, dated 31st March 2007 showing Chilika lagoon (A), deep sea (B), forestry (C) and bare/ cultivated soil (D). (b) Average noemalized DN values for vegetation (C) and soil (D) zones

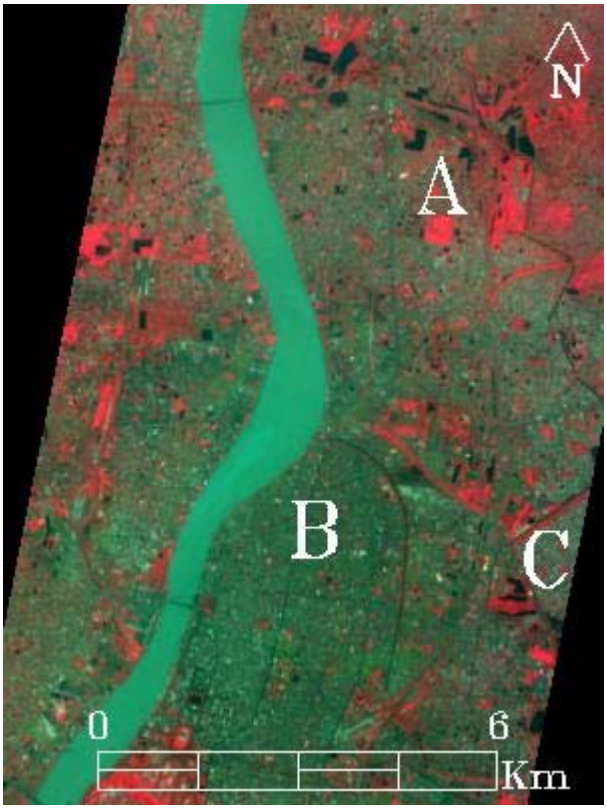

(a)

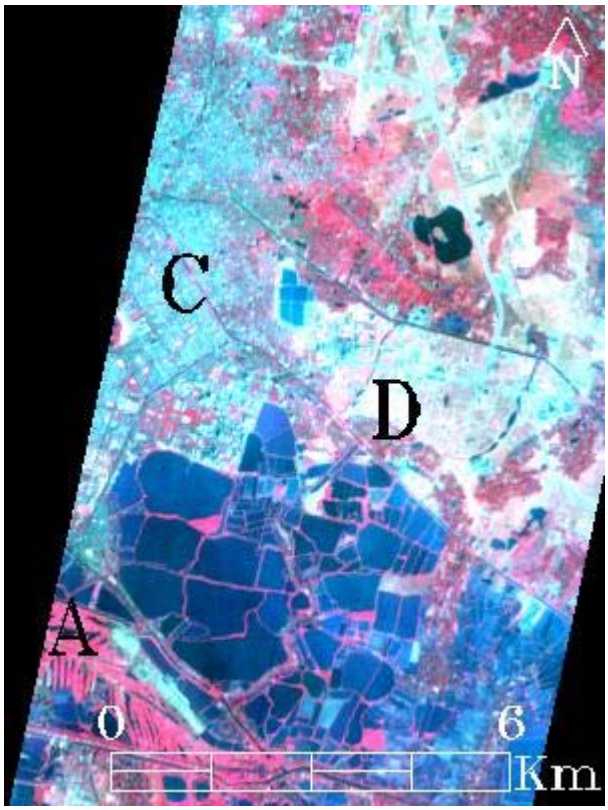

(b)

Figure 6: Hyperion image composed of bands 42, 32 and 21 for Kolkata (22°35′ N, 88°24′ E) : (a) for rainy season (July 27, 2002) and (b) for winter season (January 06, 2010).

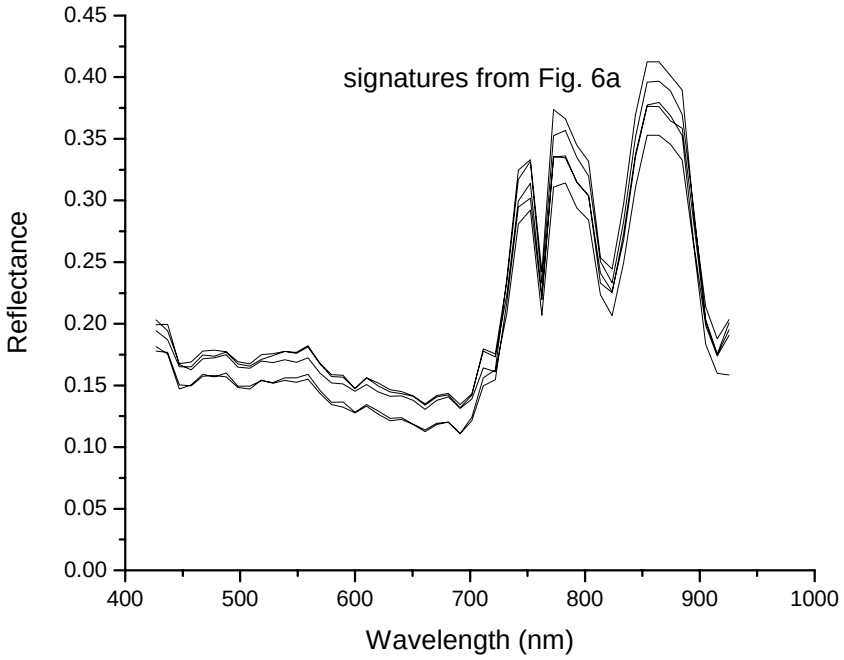

(a)

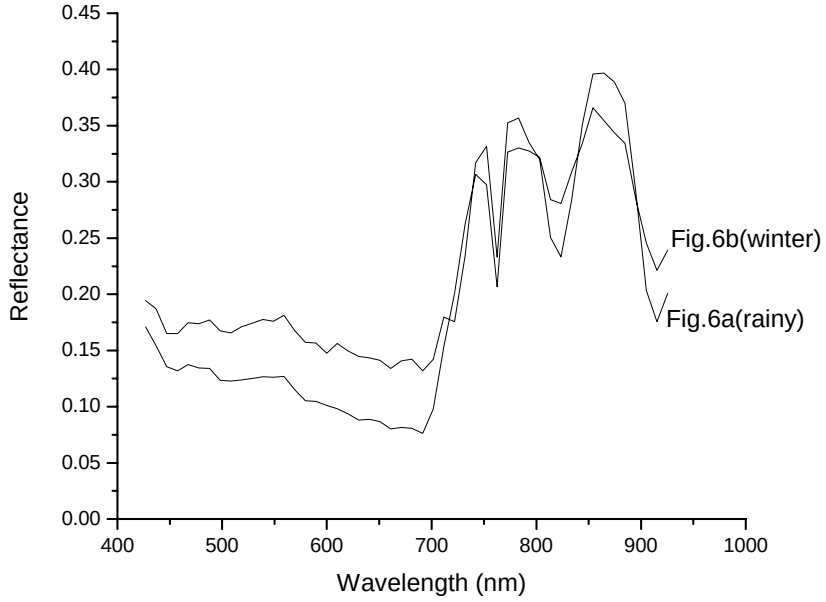

(b)

Figure 7: Vegetation signatures extracted from hyperion images: (a) from figure 6*a*, (b) from figures 6*a* and 6*b* compared, (c) normalized solar irradiance in rainy and winter seasons showing the change in oxygen and water vapour absorption (d) laboratory signature of vegetation is compared with vegetation signatures extracted from figures 6*a* and 6*b* eliminating the oxygen and water vapour absorption bands.

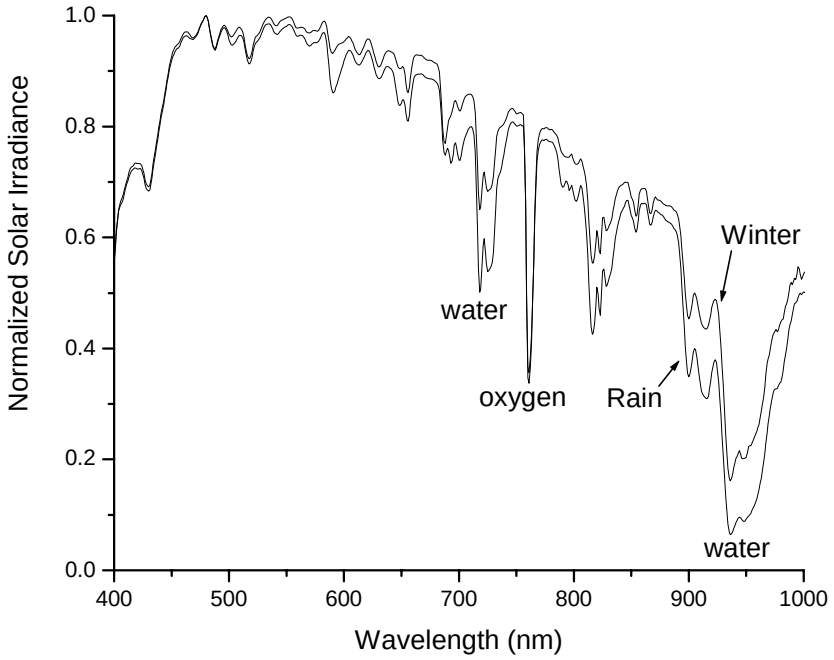

(c)

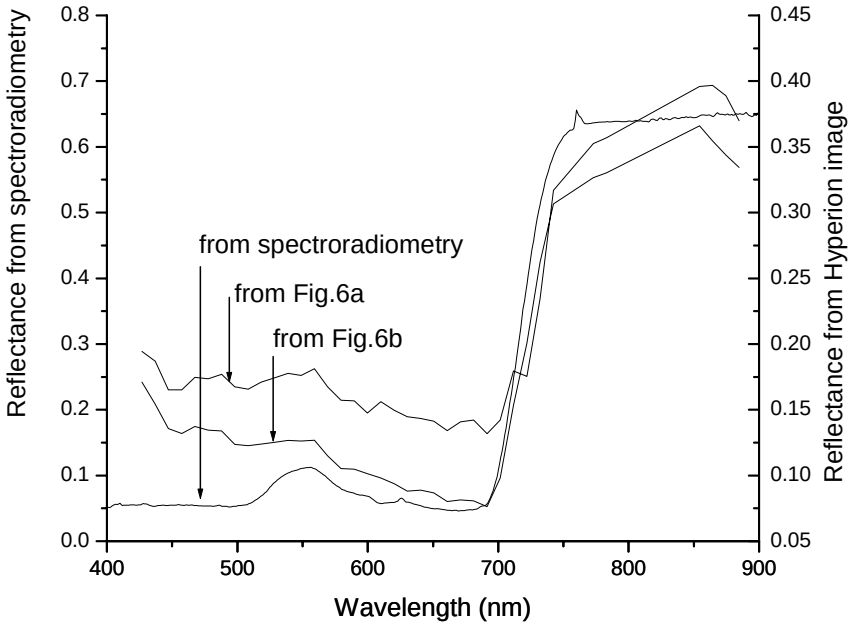

(d)

Figure 7: Vegetation signatures extracted from hyperion images: (a) from figure 6*a*, (b) from figures 6*a* and 6*b* compared, (c) normalized solar irradiance in rainy and winter seasons showing the change in oxygen and water vapour absorption (d) laboratory signature of vegetation is compared with vegetation signatures extracted from figures 6*a* and 6*b* eliminating the oxygen and water vapour absorption bands.

Figure 7(c) clearly denotes the actual positions of these absorption bands in solar irradiance spectrum measured with the present work. In the next step, the channel Nos. 40, 41, 45 to 48 and 54 to 57, corresponding to the oxygen and water vapour absorptions were eliminated. The signatures were generated with the remaining channels and compared with the laboratory-derived signature, as shown in figure 7(d). It is apparent that although there is difference in the absolute values of reflectance, the nature of spectral variation is the same in both laboratory and satellite-derived data. It indicates that it is possible to imitate the signature obtained from satellite image with a rigorous and methodical establishment of spectral library. Also the library can help to predetermine the suitable channels of the satellite and reduce the number accordingly.

The zones ‘B’ and ‘C’ of figure 6(a) are not as pure as vegetated zones like ‘A’. It has been verified by ground survey that zone-B is highly populated area consisting of concrete and asphalt and very less amount of vegetation. Zone-C is a part of well-planned township consisting of uniformly distributed concrete and asphalt and containing larger quantity of vegetation in garden, roadside etc. The spectral signatures derived from several randomly chosen pixels of zone-B are shown in figure 8(a). The oxygen and water absorption bands are similar to those of figure 7(a). Eliminating these bands, as mentioned earlier, the sample signatures of zones A, B and C are generated and plotted in figure 8(b). The change in the quantity of vegetation is obvious in the NIR region. Figure 8(c) shows the curves generated by linear combination of concrete (Conc), asphalt (Asph) and vegetation (Veg) signatures in different proportions indicated against the curves. The asphalt signature was taken from JHU spectral library and the rest were generated with the present work. Comparing figures 8(b) and 8(c), it is understood that the relative weights of endmembers in satellite image can be imitated by laboratory spectra and their permutation-combination.

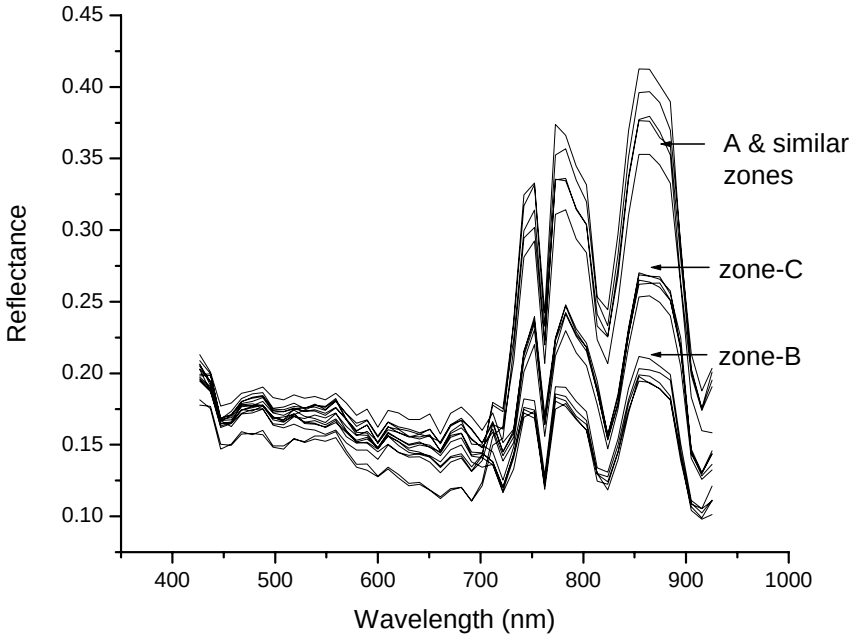

(a)

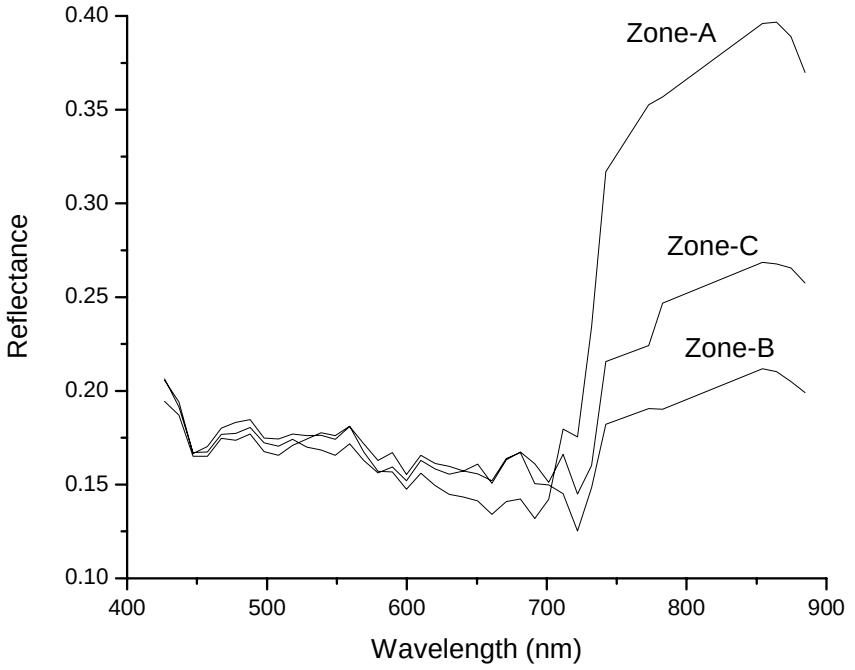

(b)

Figure 8: (a) The spectral signatures derived from several randomly chosen pixels of zones 'A', 'B' and 'C' of figure 6*a* (b) the same signatures after eliminating the oxygen and water vapour absorption bands (c) signatures generated by linear combination of concrete (Conc), asphalt (Asph) and vegetation (Veg) reflectance in different proportions indicated against the curves.

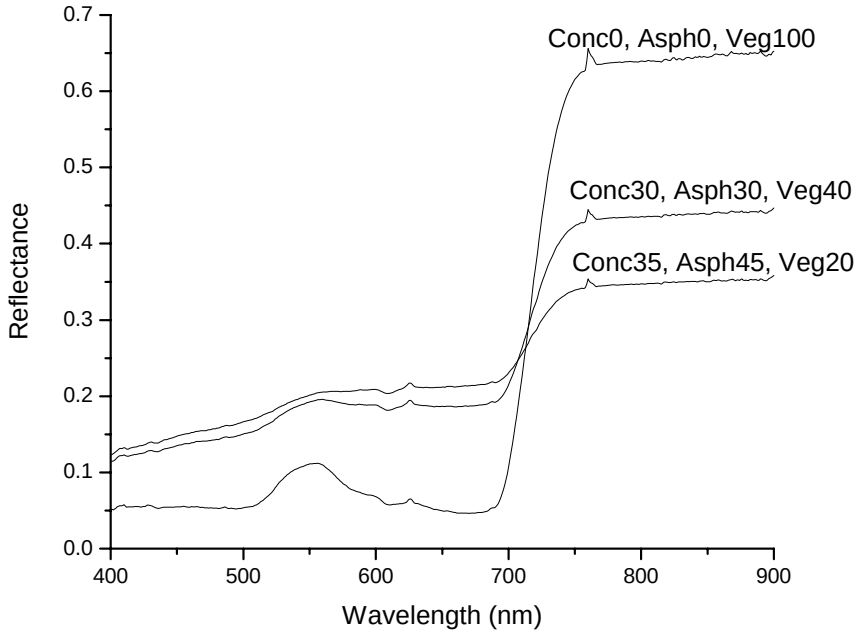

(c)

Figure 8: (a) The spectral signatures derived from several randomly chosen pixels of zones 'A', 'B' and 'C' of figure 6*a* (b) the same signatures after eliminating the oxygen and water vapour absorption bands (c) signatures generated by linear combination of concrete (Conc), asphalt (Asph) and vegetation (Veg) reflectance in different proportions indicated against the curves.

Figure 9(a) shows the spectral signatures derived from several randomly chosen pixels of zone-D of figure 6(b). Such zones consist of slum housings with terracotta tile roofs, as noted from ground observation. Figure 9(b) compares one such signature with that obtained from zone-C, the absorption bands being removed in both. This zone-C is the counterpart of that in figure 6(a) with a time gap of almost eight years. The temporal change during this span is not studied here. However, it is clear that zones D and C distinguishable signatures. Zone-D mainly consists of terracotta whereas zone-C consists of concrete, both mixed with some amount of soil and vegetation. The spectral signature of terracotta was verified in laboratory and was found to exhibit the same nature as that of brick within the UV-vis-NIR range. Therefore, it is not separately shown. Pure terracotta has lower value of reflectance than that of pure concrete within the visible region, as may be understood from the comparison of brick and concrete in figure 1(a). A similar feature is noted in figure 9(b) too. However, the NIR reflectance of zone-D has exceeded that of

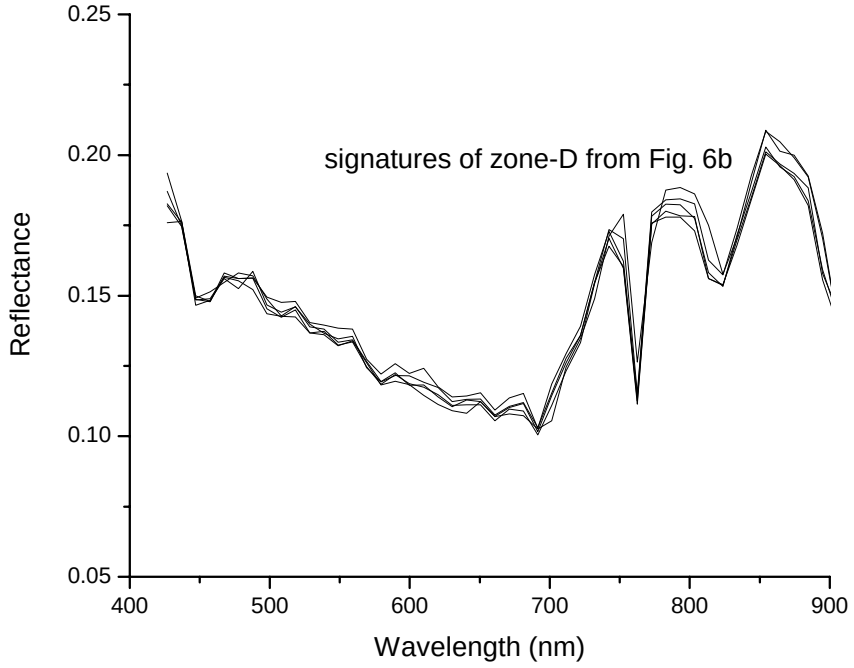

(a)

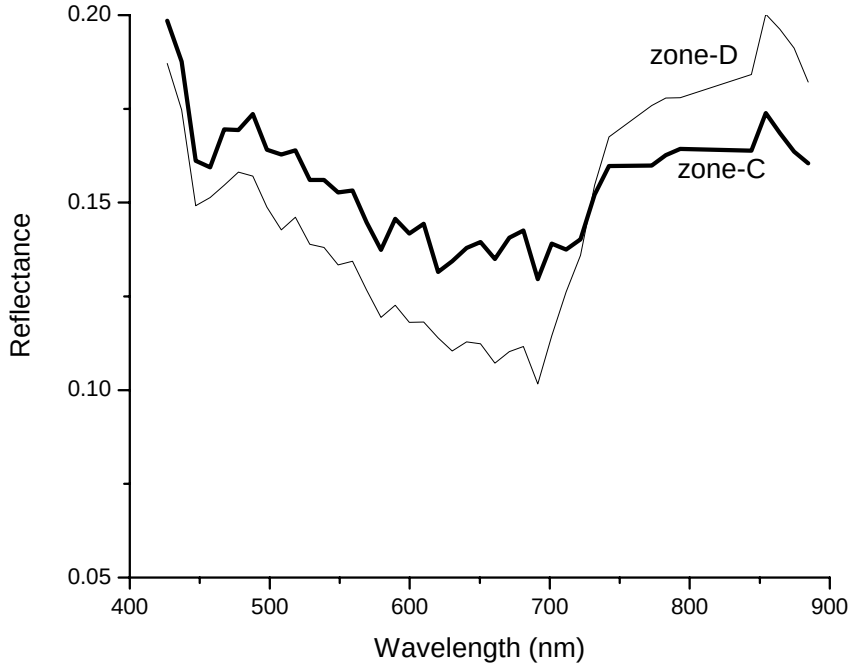

(b)

Figure 9: The spectral signatures derived from several randomly chosen pixels of zone-D of figure 6*b* (b) a sample signature of zone-D is compared with that of zone-C after eliminating the oxygen and water vapour absorption bands in both (c) some laboratory signatures of mixtures of concrete (Conc), asphalt (Asph), terracotta (TC), soil and vegetation (Veg), the proportions being indicated against the curves.

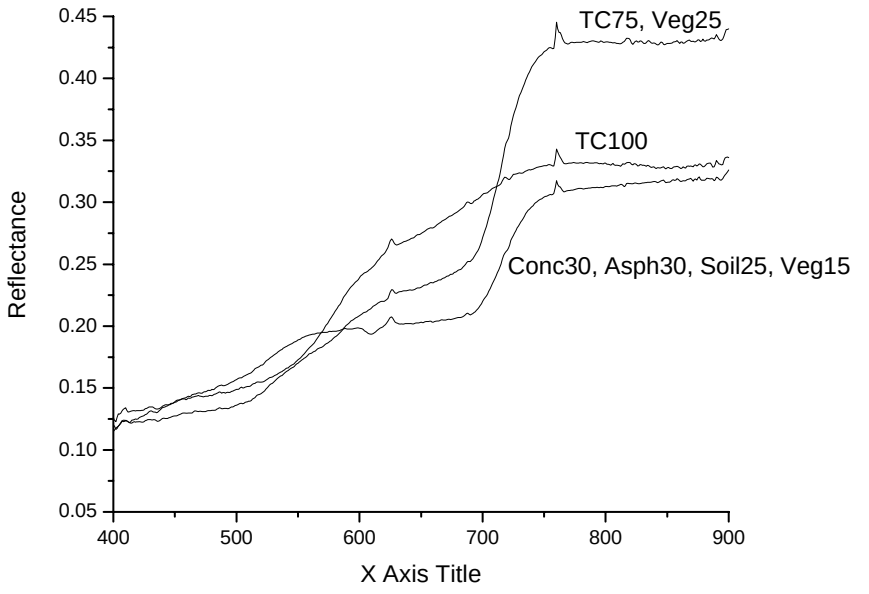

(c)

Figure 9: The spectral signatures derived from several randomly chosen pixels of zone-D of figure 6*b* (b) a sample signature of zone-D is compared with that of zone-C after eliminating the oxygen and water vapour absorption bands in both (c) some laboratory signatures of mixtures of concrete (Conc), asphalt (Asph), terracotta (TC), soil and vegetation (Veg), the proportions being indicated against the curves.

zone-C, which might be due to larger quantity of vegetation involved in the former. In order to guess the situation of figure 9(b), figure 9(c) generates some laboratory signatures with possible mixtures of concrete (Conc), asphalt (Asph), terracotta (TC), soil and vegetation (Veg). It is noted that a mixture somewhere between pure TC (100%) and TC 75% plus Veg 25% may produce spectral variation similar to that of zone-D in figure 9(b) having lower visible and higher NIR reflectance than that of a mixture of (Conc 30% plus Asph 30% plus soil 25% plus Veg 15%), a possible mixture of zone-C. Thus it is understood that with certain combination of the endmembers, the laboratory signature can imitate the satellite-derived signature.

1.4. Conclusion

The present work suggests a reverse method of standardizing the mixed pixel spectral response for a certain distribution of endmembers by synthesizing spectra with varying proportions of spectral library data and matching them with the experimental result. This

idea is demonstrated with a simple model having linear combination of endmembers. In one phase of the work, model pixels (pure and mixed) were generated in laboratory with different proportions of endmembers, *viz*. concrete, brick, moist soil and vegetation and hyperspectral reflectance measurements were carried out with them. The results were compared with computationally generated data synthesized by linear mixing of pure spectral signatures. Good matching in spectral variation was obtained in most cases. In the other phase of the work, hyperspectral signatures derived from hyperion images were compared with laboratory signatures. The trends of spectral variation were found to be the same in both cases.

The present work is a model to support the idea of spectral synthesis and it needs further developments both in computational techniques and generating spectral libraries. The constituent original spectra used for synthesizing the mixed spectra should be very accurate incorporating all possible variations. The present work was demonstrated with only one set of data for each endmember and simple linear mixing of them.

However, the merit of such technique is that the image need not be the sole resource of information. The basic idea is to compare the image spectrum with the spectral library, where the reflectance quality is assured. Thus the computational job is increased with the advantage of comparison even with an optimal number of satellite spectral bands. In fact, such sampling of optimal subset of the complete set of hyperspectral bands has been suggested earlier in the context of feature classification (Serpico and Bruzzone 1994). Therefore the keen perfection, hence the technological complicacy of the satellite sensor may be a bit compromised with optimization in band selection thereby reducing the data volume and transmission bandwidth.

REFERENCES

ALBEROTANZA, L., BRANDO, V. E., RAVAGNAN, G. and ZANDONELLA, A., 1999, Hyperspectral aerial images. A valuable tool for submerged vegetation recognition in the Orbetello Lagoons, Italy, *International Journal of Remote Sensing*, **20**, pp. 523–533.

BOREL, C C. and GERSTL, S. A., 1994, Nonlinear spectral mixing models for vegetative and soils surface, *Remote Sensing of Environment*, **47**, pp. 403 – 416.

BRANDO, V. E. and DEKKER, A. G., 2003, Satellite hyperspectral remote sensing for estimating estuarine and coastal water quality, IEEE Tranactions on Geoscience and Remote Sensing, **41**, pp. 1378–1387.

CHANG, C. -I., (Ed.), 2007, *Hyperspectral Data Exploitation: Theory and Applications*, John Wiley & Sons, Inc., New Jersey & Canada.

HOWARI, F. M., GOODELL, P. C. and MIYAMOTO, S., 2002, Spectroscopy of salts common in saline soils. In R.S. Muttiah (Ed.), *From laboratory spectroscopy to remotely sensed spectra of terrestrial ecosystems,* chapter–1 (pp. 1–20) Dordrecht: Kluwer Academic.

KWON, H and NASRABADI, N. M., 2005, Kernel RX-algorithm: A nonlinear anomaly detector for hyperspectral imagery, *IEEE Transactions on Geoscience and Remote Sensing*, **43**, pp. 388–397.

MANOLAKIS, D., SIRACUSA, C. and SHAW, G., 2001, Hyperspectral subpixel target detection using linear mixing model, *IEEE Transactions on Geoscience and Remote Sensing*, **39**, pp. 1392–1409.

MAZER, A. S., MARTIN, M., LEE, M and SOLOMON, J. E., 1988, Image processing software for imaging spectrometry data analysis, *Remote Sensing of Environment*, **24**, pp. 201–210.

MISHRA, A. K., DADHWAL, V. K. and DUTT, C. B. S., 2008, Analysis of marine aerosol optical depth retrieved from IRS-P4 OCM sensor and comparison with the

aerosol derived from SeaWiFS and MODIS sensor, *Journal of Earth System Science*, **117**, pp. 361–373.

MOORHEAD, I. R., GILMORE, M. A., HOULBROOK, A. W., OXFORD, D. E., FILBEE, D., STROUD, C., HUTCHINGS, G. and KIRK, A., 2001, CAMEO-SIM: a physics-based broadband scene simulation tool for assessment of camouflage, concealment, and deception methodologies, *Optical Engineering*, **40**, pp. 1896–1905.

NOLIN, A.W. and DOZIER, J., 2000, A hyperspectral method for remotely sensing the grain size of snow, *Remote Sensing of Environment*, **74**, pp. 207–216.

PANFEROV, O., KNYAZIKHIN, Y., MYNENI, R. B., SZARZYNSKI, J., ENGWALD, S., SCHNITZLER, K. G. and GRAVENHORST, G., 2001, The role of canopy structure in the spectral variation of transmission and absorption of solar radiation in vegetation canopies, *IEEE Transactions on Geoscience and Remote Sensing*, **39**, pp. 241–253.

SALEM, F., KAFATOS, M., EL-GHAZAWI, GOMEZ, R. and YANG, R. X., 2005, Hyperspectral image assessment of oil-contaminated wetland, *International Journal of Remote Sensing*, **26**, pp. 811–821.

SERPICO, S. B. and BRUZZONE, L., 1994, A new search algorithm for feature selection in hyperspectral remote sensing images, *IEEE Transactions on Geoscience and Remote Sensing: Special Issue on Analysis of Hyperspectral Image Data*, **39**, pp. 1360–1367.

SETTLE, J. J., 1996, On the relationship between spectral unmixing and subspace projection, *IEEE Transactions on Geoscience and Remote Sensing*, **34**, pp. 1045–1046.

VARSHNEY, P. K. and ARORA, M. K. (Eds.), 2004, *Advanced Image Processing Techniques for Remotely Sensed Hyperspectral Data*, Springer-Verlag, Berlin.

ZARCO-TEJADA, P. J., USTIN, S. L. and WHITING, M. L., 2005, Temporal and spatial relationships between within-field yield variability in cotton and high-spatial hyperspectral remote sensing imagery, *Agronomy Journal*, **97**, pp. 641–653.

PART-II: DEMONSTRATION OF SIGNATURE CAMOUFLAGE

In course of experiment, it was noted that an endmember, after acquiring a certain large portion of majority in the field of view, dominated the spectral response and resembled 100% contribution. If the existence of an object went below a critical area, it was concealed in the spectral response. The above finding is important to low spatial resolution hperspectral image because it can be either a limitation in identification of object or deliberate exploitation in camouflaging objects. It has been demonstrated with the following experiment.

The spectroradiometer (25° FOV) was hung vertically downward at a height of 2.5 m over a concrete surface exposed to full sun at around solar noon, taking care of self-shadowing. An area of 1.5 m×1.5 m of the concrete surface, considered as a single pixel, was gradually covered with banana leaves. The photographs of Figure 10 explain the situation. The bare surface is designated ‘A’. Then B, C and D represent the gradually increasing vegetation covers, D being the full cover. The corresponding spectral curves are shown in Figure 11. It is noted that as the concrete surface is fully covered with vegetation (D), the signature resembles that of vegetation. But the presence of little vegetation (B) is hardly distinguishable from bare surface (A).

Again, the leaves were gradually removed (E and F) from the full leaf-covered surface (D). The corresponding spectral curves are shown in Figure 12. It is noted that the presence of the little exposed concrete surface (E) is hardly distinguishable from full cover (D). Thus the presence of little amount of an endmember within larger amount of another endmember remains undetected by the hyperspectral sensor.

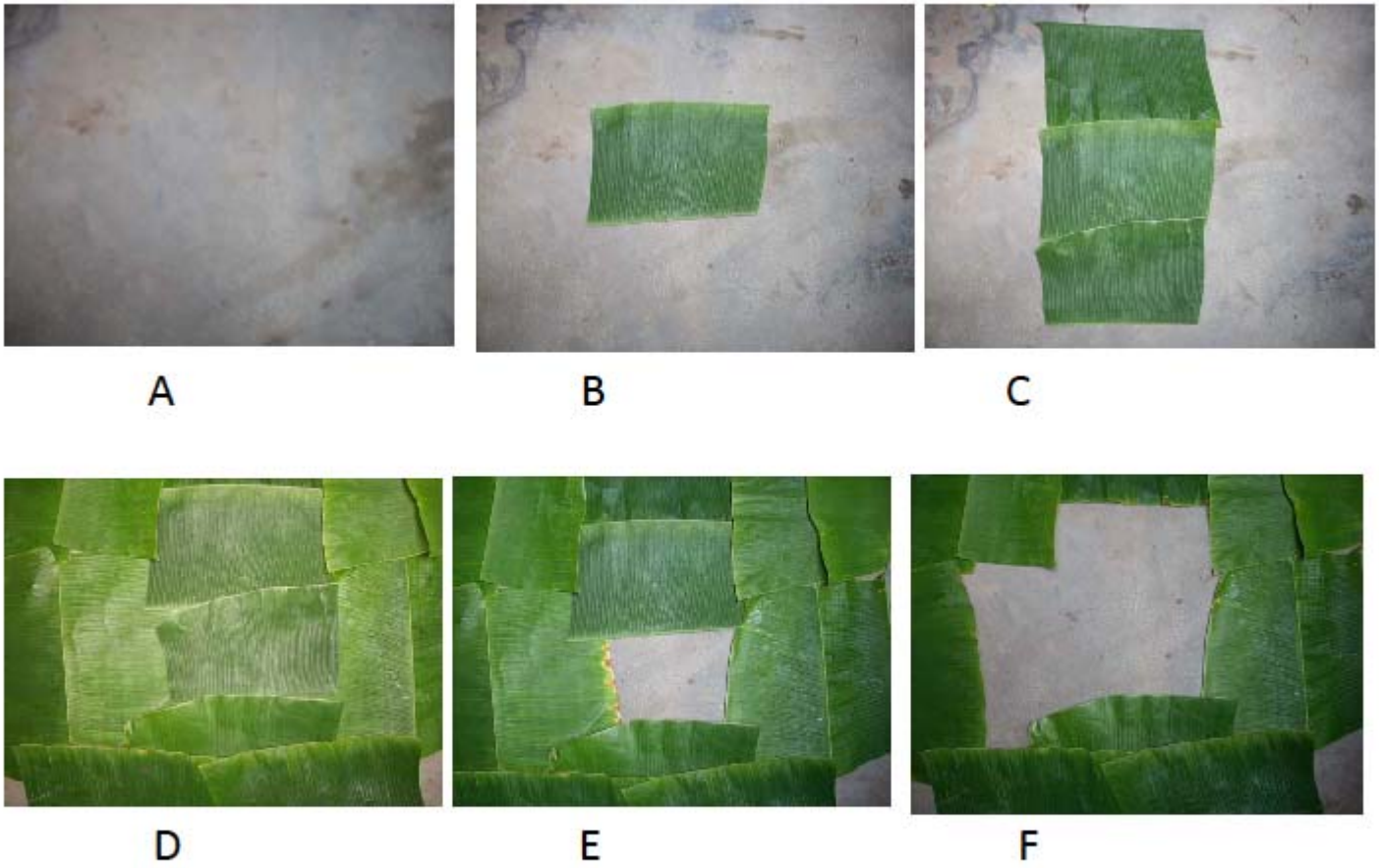

Figure 10. Gradual covering of bare concrete surface (A) with banana leaves (B, C and D) and removal (E and F)

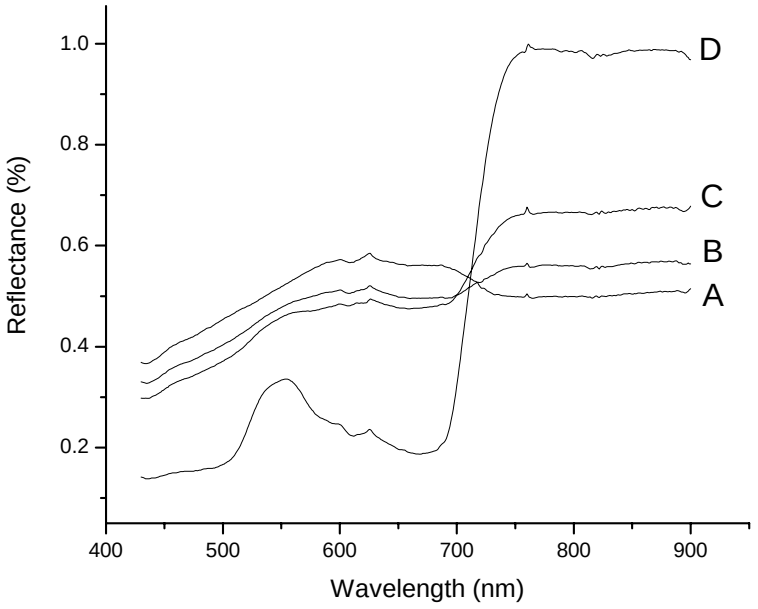

Figure 11. Change of spectral response during increasing banana leaf portion from bare concrete (A) to full leaf cover (D)

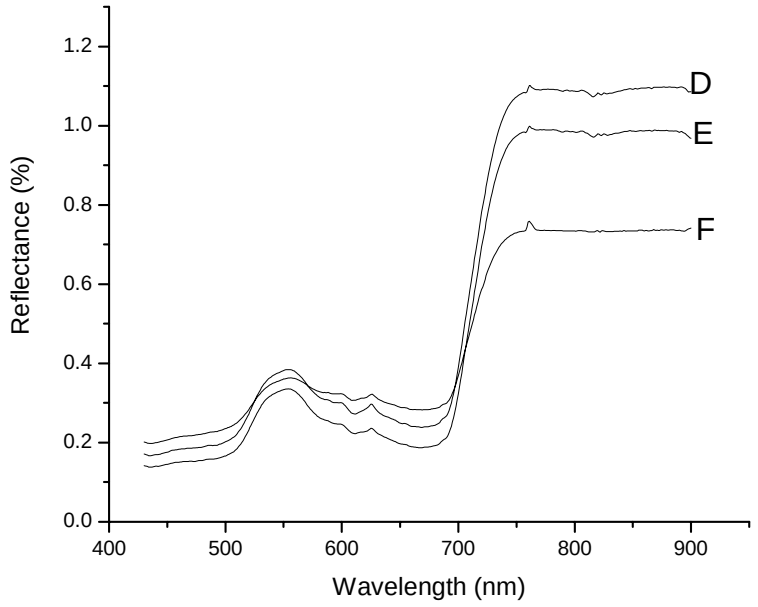

Figure 12. Change of spectral response during decreasing banana leaf portion from full cover (D) condition

PART-III: SOLAR IRRADIANCE STUDIES

The present work investigates on the diurnal, seasonal and atmospheric variations of the atmospheric oxygen absorption (O_2 – A) band depth, a hyperspectral signature at around 760 nm of the solar radiation spectrum useful to the remote sensing of a lot of atmospheric and surface features. The conditions of the band at full-moon night and at solar eclipse are also studied. It is noted that the O_2 – A band depth is retained even at 90% sun cover of solar eclipse and at lunar illumination, which indicates that the advantage of this absorption may be obtained with any source emitting radiation around 760 nm even in the absence of the sun, *i.e.* at night. The change in optical depth due to diurnal and seasonal variations are studied and compared. The presence of aerosol is found to strongly influence the band depth so that the aerosol optical depth can be estimated from this band. This has been justified from both ground based hyperspectral spectroradiometric measurements and Hyperion hyperspectral satellite image analysis.

3.1. Introduction

The narrow band of atmospheric oxygen absorption (O_2 – A) at around 760 nm in the solar radiation spectrum is a good hyperspectral signature for the remote sensing of a lot of atmospheric and surface terrestrial features. For instance, cloud top height is estimated from backscattered radiance within O_2 – A band (Fischer and Grasl 1991). Retrieval of cloud fraction and cloud top pressure over desert zone with reflectance measurement in this band is reported (Koelemeijer *et al.*2001, Fournier *et al.* 2006). The diffused transmittance in this band is used to obtain the effective air mass in connection with the estimation of water vapor column (Kiedron *et al.* 2003). Land surface pressure is retrieved from satellite data covering this band (Dubuisson *et al.* 2001, Ramon *et al.* 2003). Fluorescence exhibited by chlorophyll of vegetation is a good spectral tool for measuring photosynthesis activity (Govindgee 2004). The oxygen absorption bands of 687 and 760 nm are close to chlorophyll fluorescence peaks at 690 and 740 nm, respectively. Therefore, the partial filling up of the O_2 – A depth due to fluorescence emission has been studied in a number of occasions (Kebabian *et al.* 1999, Moya *et al.* 2004, Liu *et al.* 2005, Meroni *et al.* 2006) including airborne imagery in this band (Zarco-

Tejada *et al.* 2009). Also that band is useful to in-flight spectral calibration of satellite (Delwart *et al.* 2007).

Looking towards the above potentials of the oxygen absorption band depth, the present work investigates on the assessment of aerosol optical depth from this absorption. There are man-made aerosols, such as carbonaceous particles and concrete dust and natural aerosols like volcanic dust and ocean salt. They play important role in atmospheric radiation balance by reflecting incoming solar radiation (albedo effect) and by arresting the outgoing terrestrial radiation (greenhouse effect). Marine aerosols promote cloud formation.

The estimation of optical depth from multispectral satellite data is well studied (Pandya *et al.* 2002, Mishra *et al.* 2008, Fraser 1995, Dey and Singh 2002). The sharp shape of the oxygen absorption band enables a hyperspectral instrument, like the one used in the present work, to precisely measure the absorption peak at different atmospheric conditions on the ground surface. Correspondingly hyperspectral satellite images are hoped to yield better information on the variation of the O_2 – A band depth. The present work studies the variation and stability of the band depth with diurnal, seasonal and atmospheric changes and also with the reduction of solar illumination, *e.g.* during night time and solar eclipse condition.

3.2. Methodology

The work consists of ground based hyperspectral radiometric measurements and hyperspectral satellite image analysis. Solar irradiance spectrum at ground surface was measured at 1 nm resolution throughout the ultraviolet-visible-near-infrared (UV-Vis-NIR) range with ASD FieldSpec spectroradiometer fitted with remote cosine receptor on 25º field-of-view fiber and kept facing vertically upward irrespective of the solar elevation. One such spectrum is plotted in Figure 13. Data were collected at different seasons and different atmospheric conditions placing the instrument at the same place and height of open air. Generally the measurements were taken at around solar noon. However, for the investigation on the diurnal changes, the measurement was conducted at the required time.

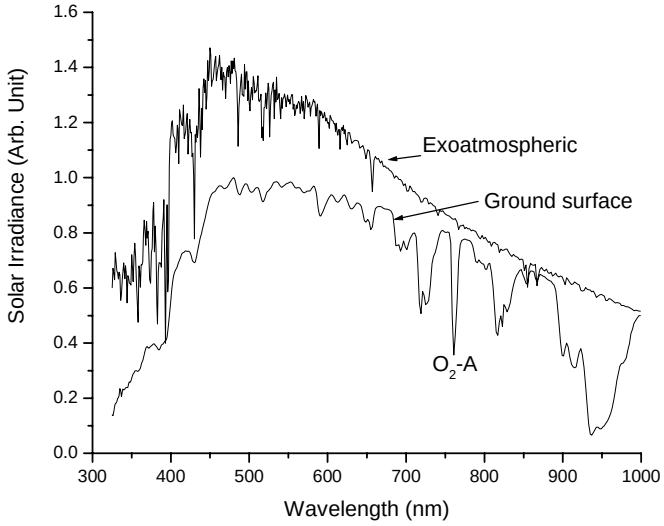

Figure 13: Solar irradiance spectrum over ultraviolet-visible-near-infrared (UV-Vis-NIR) range of wavelength measured at ground surface compared with the corresponding exoatmospheric irradiance variation

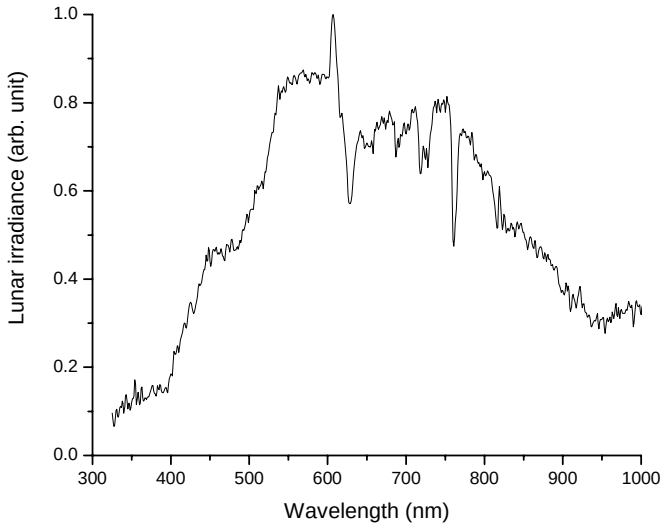

Figure 14: Lunar irradiance spectrum obtained during full moon.

Measurement with the above set up was carried out at night time also during full moon. The result is shown in Figure 14. Also the solar irradiance was measured during solar eclipse occurred on the 22nd July, 2009 morning from a place of Kolkata (22°39′N, 88°23′E) in order to observe the possible changes in the oxygen absorption during the

glooming of solar intensity at sun covering up to almost 90%. The variation of the solar irradiance spectrum during the eclipse is presented in Figures 15 (a) and (b).

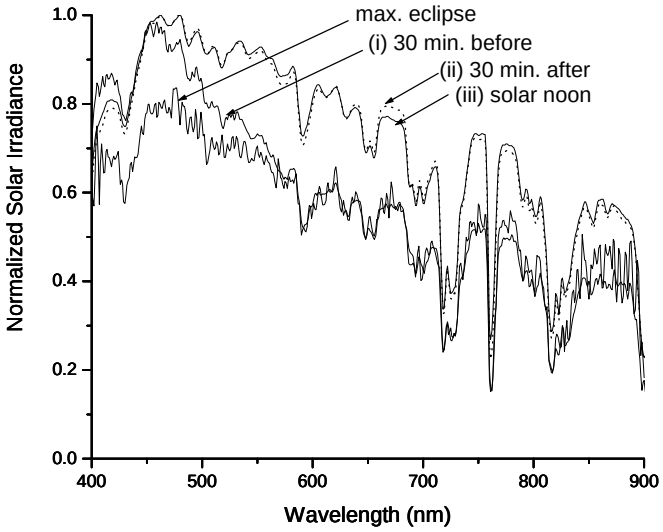

(a)

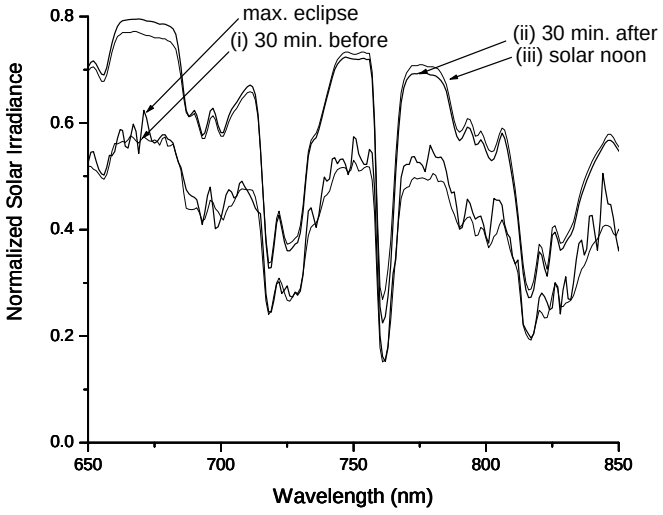

(b)

Figure 15: Variation of solar irradiance during solar eclipse (a) throughout the UV-Vis-NIR region, (b) the NIR portion enlarged. The maximum eclise condition is compared with that at (i) 30 minutes before, (ii) 30 minutes after and (iii) full sun

Also the reflected solar radiance for vegetation was measured with 25º field-of-view removing the remote cosine receptor and facing the instrument vertically downward over the surface. To simulate the effect of uniform vegetation canopy, fresh large banana

leaves were spread over horizontal surface. The measurement was calibrated with Spectralon white reference panel.

The wavelength (λ) dependent radiation intensity (I_λ) at the ground surface and that at the top of the atmosphere ($I_{0\lambda}$) as function of optical depth (τ_λ), as related by Beer-Bouguer-Lambert law, does not hold for strong gaseous absorption region. However, the advantage is the precise, universal location of the absorption band in the spectrum. Even it were some unknown function of optical depth, such as

$$I_\lambda = I_{0\lambda} f(\tau_\lambda) \qquad (2)$$

the knowledge of the ratio of the absorption maximum to the baseline (average of the two points on both sides of the band) at different conditions would yield a value proportional to the optical depth. The results in the present work are compiled in Table-2.

The satellite images were analyzed using ENVI 4.5 image processing software. Hyperion hyperspectral images (ground resolution 30 m) for Kolkata metropolis and nearby area (centred around 22°35′ N, 88°24′ E) were downloaded from USGS website. The digital number (DN) values were converted to reflectance (*R*) for fifty VNIR waveband channels (No. 8 to 57) using the formula expressed by Eq. (1).

3.3. Results and Discussion

Since the individual results are of different numerical values, the graphical variations are normalized to show the proportional variations. Figure 13 represents the relative change of irradiance variation over the UV-Vis-NIR region compared with the extraterrestrial irradiance (standard data) over the same range. Two useful features are noted there. The sharp absorption band of oxygen at 760 nm enables a hyperspectral instrument to precisely measure the absorption peak; hence hyperspectral satellite images are likely to yield better information on the oxygen absorption band depth. The extraterrestrial irradiance around 760 nm is noted to vary steadily with wavelength thereby forming a good baseline for absorption estimation.

Figure 14 represents the lunar irradiance measured at night time in full moon. The sharp oxygen absorption (O_2 – A) band is still present. Figures 15 (a) and (b) show the

change in solar irradiance spectrum during solar eclipse up to almost 90% covering. Only the change in radiation intensity is the topic of interest here. It is apparent from Figures 15 (a) and (b) that the overall solar irradiance uniformly reduces during the eclipse. However, the O_2 – A band depth retains its size and shape. The important feature understood from Figures 14 and 15 that the atmospheric absorption due to oxygen works irrespective of the intensity of illumination, solar or any other, over the atmosphere. This indicates that the feature of oxygen absorption can be achieved at night time also with any strong radiation source emitting around 760 nm.

Table-2: Comparison of optical depths obtained from ground data and Hyperion image at different atmospheric conditions

Atmospheric conditions and mode of measurement	From ground based measurements								From Hyperion Images	
	Effect of aerosol		Seasonal changes				Time after sunrise			
	Before rain	After rain	sunny	cloudy	summer	winter	90 mins.	360 mins.	winter	rainy
Optical depth	0.435	0.379	0.381	0.455	0.430	0.465	0.496	0.300	0.1084	0.1057

Figures 16 (a) and (b) justify the suitability of the O_2 – A band for aerosol optical depth estimation. The irradiance obtained in dry summer full-sun (designated as 'before rain') is compared with that obtained at full-sun after prolonged rain for 5-6 days (designated as 'after rain'). In the former case, the sky being depleted of rain for several months is expected to contain large amount of aerosol and dust particles, which are supposed to be partly flushed out in the later case. On removal of aerosols, the absorption depth is considerably decreased.

The effects of some other atmospheric changes in the O_2 – A band were also studied. Figure 17 shows the full-sun and cloud-covered conditions. In presence of cloud, the absorption depth slightly increases. Figure 18 illustrates the seasonal variation of solar irradiance.

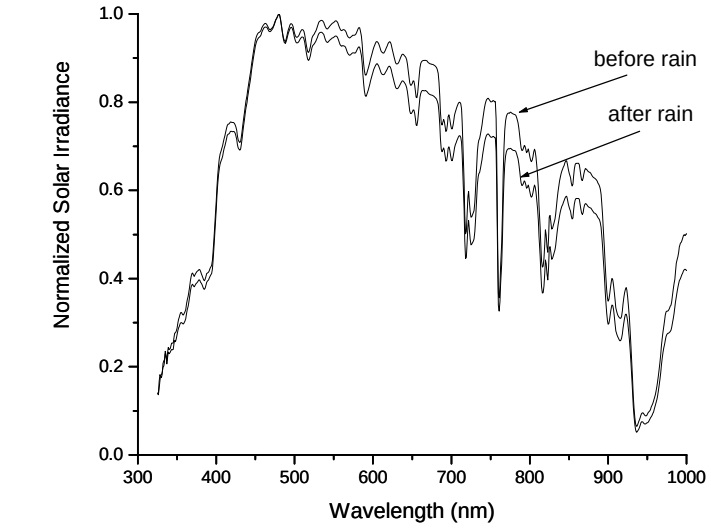

(a)

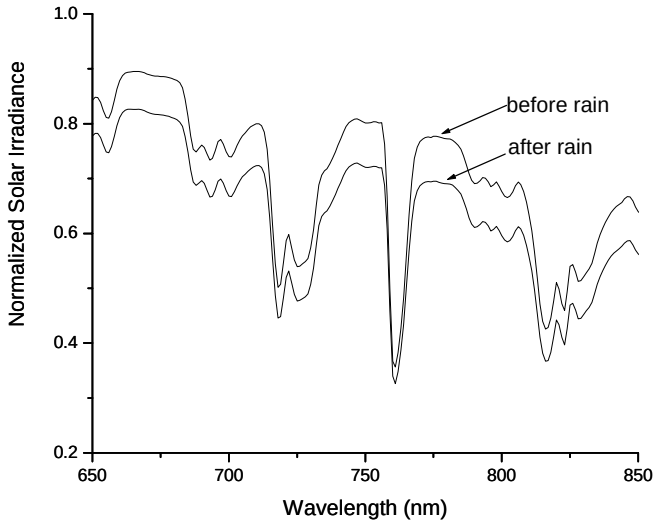

(b)

Figure 16: Comparison of solar irradiance in dry summer (before rain) with that after continuous rain (after rain) (a) throughout the UV-Vis-NIR region (b) the NIR portion enlarged

In winter season, the oxygen absorption depth slightly increases due to larger air mass originated from lager inclination of the sun. The considerable decrease in water absorption band depths on both sides of the O_2 – A band may be noted. Figure 19 shows diurnal change in the absorption band depth. Obviously the depth in the morning is larger than that at noon because of larger air mass originated from the inclination of the sun in

the morning. Table-2 compares the amount of all these change with that with aerosol related changes.

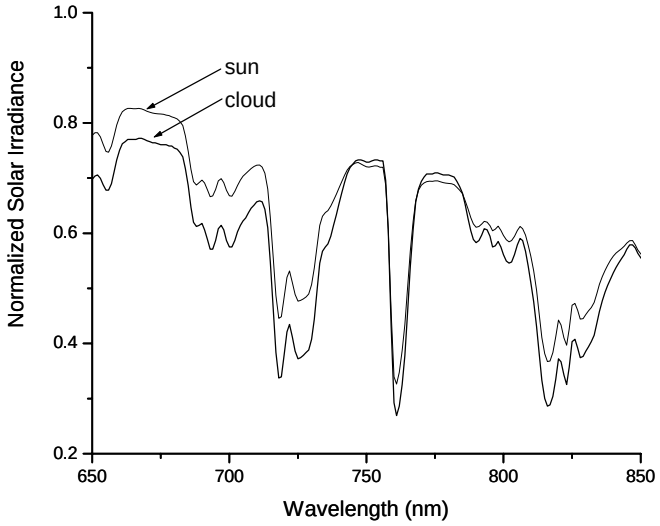

Figure 17: Comparison of solar irradiance obtained at full-sun and cloud-covered conditions enlarging the NIR region

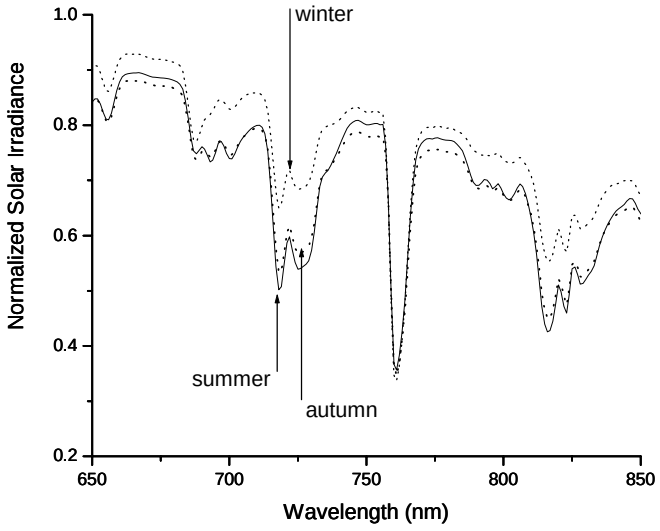

Figure 18: Seasonal variation of solar irradiance with the NIR portion enlarged

The vegetation signature was used for the interpretation because it has a typical nature and it is easily obtained in pure pixel form in the images. The spectral signatures of vegetation within the UV-vis-NIR range were derived from a number of randomly

chosen pure pixel vegetated zones of the Hyperion hyperspectral satellite images of Figure 6 (a) and (b).

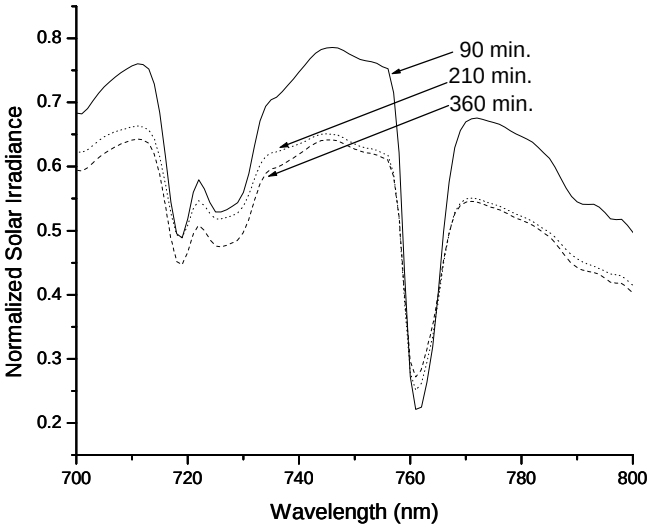

Figure 19: Diurnal change of O_2 – A band depth with the NIR region enlarged. Different times after the sunrise are indicated against the curves

Such regions are denoted by 'A' in the figures. Some other distinguishable regions are highly populated areas (B) full of concrete and asphalt, less populated urban areas (C) and slum areas (D) with terracotta roof tiles. The average vegetation spectra derived from the vegetated (A) zones of both the figures are shown in Figure 20(a). The absorptions due to oxygen around 760 nm (O_2 – A) and that due to water vapour around 810 & 900 nm can be identified on comparing with the actual positions of these absorption bands in the solar irradiance spectra of Figure 13 and Figure 18. The water vapour absorption is much reduced in winter, as noted from both Figure 18 and Figure 20(a) whereas the O_2 – A band remains almost steady. On removing the channel Nos. 40, 41, 45 to 48 and 54 to 57, corresponding to the oxygen and water vapour absorptions, the satellite-derived signatures with the remaining channels look like the laboratory-generated signature, as compared in Figure 20(b). However, the present topic of interest is the presence of the O_2 – A band. The ratio of the absorption maximum to the baseline is listed in Table-2.

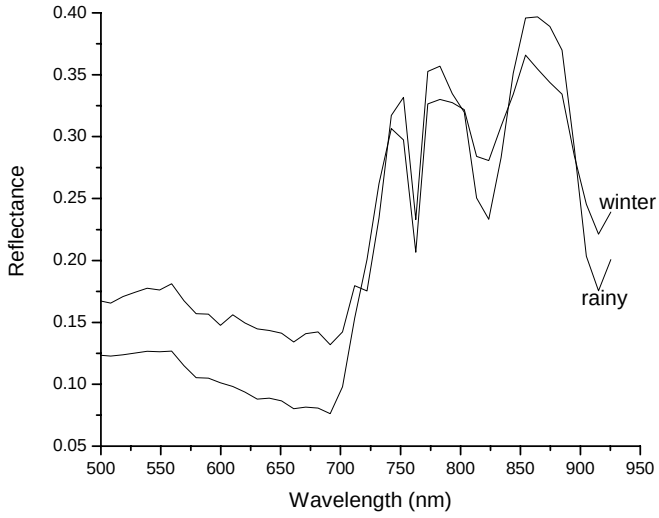

(a)

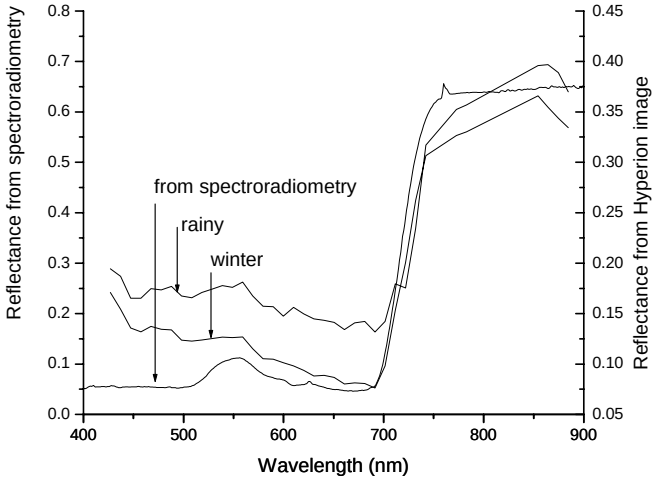

(b)

Figure 20: (a) Vegetation signatures extracted from Hyperion images of rainy [Fig. 6(*a*)] and winter [Fig. 6(*b*)] seasons and (b) those compared with the vegetation signature generated by spectroradiometry in laboratory

The suitability of aerosol measurement is justified as follows. Aerosol measurement from ground surface follows Beer-Bouguer-Lambert law

$$L_\lambda = L_{\lambda 0} \exp(-m\tau_\lambda) \tag{3}$$

The total optical depth (τ_λ) has contributions from Rayleigh scattering, Gaseous absorption, water vapour absorption and aerosol scattering. Aerosol measurement from satellite sensor is carried out as follows.

Radiance detected by the sensor (L_λ) = Radiance leaving object surface + Path radiance (aerosols + Rayleigh) (4)

Aerosol optical depth = L_λ . constant (4a)

where the constant involves extraterrestrial solar radiance, solar elevation and satellite viewing geometry. Thus the key factor in aerosol estimation is the determination of optical depth. The advantages of using O_2 – A band in determination are that the Rayleigh scattering can be neglected at 760 nm with respect to strong gaseous absorption and the fluctuation due to water vapour absorption need not be considered.

3.4. Conclusion

The present subject of investigation is the atmospheric oxygen absorption (O_2 – A) band depth at around 760 nm of the solar radiation spectrum, a useful parameter for cloud detection, chlorophyll fluorescence study and other remotely sensible features. The variations of the band depth with seasonal, diurnal and atmospheric changes and also with the reduction of the source itself, *i.e.* the sun during solar eclipse have been studied. The change in band depth at each of the above conditions is reported. The presence of aerosols is found to have predominant effect on the absorption depth.

References

1. J. Fischer and H. Grasl, “Detection of cloud-top height from backscattered radiances within the oxygen A band. Part 1: Theoretical study”, *J. Appl. Meteorology*, vol. 30, pp. 1245-1259, Sept.1991.

2. R.B.A. Koelemeijer, P. Stammes, J.W. Hovenier and J.F. de Haan, “A fast method for retrieval of cloud parameters using oxygen A band measurements from the Global Ozone Monitoring Experiment”, *J. Geophys. Res*., vol. 106, pp. 3475-3490, Feb.2001.

3. N. Fournier, P. Stammes, M. de Graaf, R. van der A, A. Piters, M. Grzegorski and A. Kokhanovsky, “Improving cloud information over deserts from SCIAMACHY Oxygen A-band measurements”, *Atmos. Chem. Phys.*, vol. 6, pp. 163–172, Jan.2006.

4. P. Kiedron, J. Berndt, J. Michalsky, and L. Harrison, “Column water vapor from diffuse irradiance”, *Geophys. Res. Lett*., vol. 30, pp. 1565-1568, June 2003.

5. P. Dubuisson, R. Borde, C. Schmechtig and R. Santer, “Surface pressure estimates from satellite data in the oxygen A-band: Applications to the MOS sensor over land”, *J. Geophys. Res*., vol. 106, pp. 27277-27286, 2001.

6. D. Ramon, L. Cazier, and R. Santer, “The surface pressure retrieval in the MERIS O_2 absorption: validation and potential improvements”, *IEEE Int. Geosc. Remote Sens. Symposium IGARSS’2003*, vol. 5, pp. 3126-28, 2003.

7. Govindjee, “Chlorophyll a fluorescence: a bit of basics and history” in *Chlorophyll a Fluorescence: A Signature of Photosynthesis: Advances in Photosynthesis and Respiration*, vol. 19, pp. 1-42, G.C. Papageorgiou and Govindjee, Eds., Springer, Dordrecht, 2004.

8. P. L. Kebabian, A. F. Theisen, S. Kallelis and A. Freedman, “A passive two-band sensor of sunlight-excited plant fluorescence” Rev. Sci. Istrument., vol. 70, pp. 4386-4393, Nov.1999.

9. I. Moya, L. Camenen, S. Evain, Y. Goulas, Z. G. Cerovic, G. Latouche, J. Flexas and A. Ounis, “A new instrument for passive remote sensing: 1. Measurements of sunlight-induced chlorophyll fluorescence”, *Remote Sens. Environ*., vol 91, pp. 186-197, May 2004.

10. L. Liu; Y. Zhang; J. Wang and C. Zhao, “Detecting solar-induced chlorophyll fluorescence from field radiance spectra based on the Fraunhofer line principle”, *IEEE Trans. Geosci. Remote Sensing*, vol. 43, pp. 827-832, April 2005.

11. M. Meroni and R. Colombo, “Leaf level detection of solar induced chlorophyll fluorescence by means of a subnanometer resolution spectroradiometer”, *Remote Sens. Environ.*, vol. 103, pp. 438-448, Aug.2006.

12. P.J. Zarco-Tejada, J.A.J. Berni, L. Suarez, G. Sepulcre-Canto, F. Morales and J.R. Miller, “Imaging chlorophyll fluorescence with an airborne narrow-band multispectral camera for vegetation stress detection”, *Remote Sens. Environ*., vol. 113, pp. 1262-1275, June 2009.

13. S. Delwart, R. Preusker, L. Bourg, R. Santer, D. Ramon, and J. Fischer, “MERIS in-flight spectral calibration”, *Int. J. Remote Sensing*, vol. 28, pp. 479-496, Jan. 2007.

14. M. R. Pandya, R. P. Singh, K. R. Murali, P. N. Babu, A. S. Kirankumar and V. K. Dadhwal, “Bandpass Solar Exoatmospheric Iradiance and Rayleigh Optical thickness of Sensor On Board Indian Remote Sensing Satellites – 1B, -1C, -1D, and P4”; *IEEE Tran. Geosci. Reomte Sensing*, vol. 40, pp. 714-718, Mar.2002.

15. K. Mishra, V. K. Dadhwal and C. B. S. Dutt, “Analysis of marine aerosol optical depth retrieved from IRS-P4 OCM sensor and comparison with the aerosol derived from SeaWiFS and MODIS sensor”, *J. Earth Syst. Sci.*, vol. 117, pp. 361–373, July 2008.

16. R. S. Fraser, “The effect of oxygen absorption on band-7 radiance” in *SeaWiFS Technical Report Series: Case Studies for SeaWiFS Calibration and Validation, Part 3*, NASA Tech. Memo.104566, S. B. Hooker, E. R. Firestone and J. G. Acker, Eds., vol. 27, pp. 16-19, 1995.

17. S. Dey and R. P. Singh, “Retrieval of aerosol parameters using IRS P4 OCM data over the Arabian Sea and the Bay of Bengal”, Current Sc., vol. 83, pp. 1235-1240, Nov. 2002.

PART-IV: CHLOROPHYLL FLUORESCENCE ESTIMATION

The present work identifies the hyperspectral fluorescence signature of chlorophyll as a small spike on the reflectance spectral curve of vegetation at the oxygen absorption band around 760 nm and investigates on the presence or absence of the spike. It justifies the origin of the fluorescence signature in the reflection spectrum with both leaf level and pigment level studies on green and senescent leaves and proposes a quantitative estimation for the filling up of the absorption band depth. The possibility of presence or absence of the spike on the reflectance curve is explained. The oxygen absorption band is available with solar radiation only because that passes through the atmospheric oxygen column. The present work outlines a prototype instrumental set-up for producing the oxygen absorption band artificially in laboratory to get the advantage of this absorption in absence of solar illumination.

4.1. Introduction

The spectrum of solar radiation penetrating the atmosphere consists of a sharp, deep absorption band caused by the atmospheric oxygen at around 760 nm, popularly known as O_2 –A band. It is an efficient tool in the field of remote sensing for the estimation of a lot of atmospheric and surface terrestrial features, such as cloud parameters [1-3], water vapor column [4] and land surface pressure [5,6]. The present work deals with the determination of another important terrestrial feature, namely vegetation fluorescence using O_2 –A band.

Chlorophyll, the green plant pigment molecule exhibits fluorescence emission of radiation at around visible red and near-infrared wavelengths when excited by shorter wavelength radiation [7, 8, 9]. It is a good spectral tool for measuring photosynthesis activity and indicator of vegetation physiological parameters like chlorophyll content [10] and plant stress [11, 12]. Studies on chlorophyll fluorescence can be carried out either *in vitro*, with extracted pigment solutions in laboratory under suitably controlled specific excitation radiation [13] or *in vivo*, with living terrestrial plants [12, 14, 15] and marine phytoplanktons [16]. The *in situ* observation of chlorophyll fluorescence at natural condition under solar illumination offers a non-destructive spectroscopic testing method

for plant physiology and adds a dimension of potential to the field of remote sensing [17-19]. It provides with large area estimation of photosynthesis activity and plant physiological conditions.

Since the fluorescence signal is very weak, the main problem of observing solar induced fluorescence of vegetation is its being masked with bright sunshine. To observe fluorescence, one has to somehow attenuate the solar radiation. One way out is the use of solar Fraunhofer lines, which match with the fluorescence emission wavelengths [17]. However, such fine resolution of wavelength (less than 0.1 nm) is very difficult to be achieved from large distance in space. An alternative is sought with atmospheric absorption bands. The most promising one is the oxygen absorption (O_2 –A) band at 760 nm. The oxygen absorption bands of 687 and 760 nm are close to chlorophyll fluorescence peaks at 690 and 740 nm, respectively. Therefore, the partial filling up of the absorption depth at 760 nm due to fluorescence emission has been studied in a number of occasions [12, 14, 20, 21].

The present work investigates on the presence or absence of fluorescence signature found in the reflection spectrum of vegetation at the O_2 –A band around 760 nm. Both leaf level and pigment level measurements have been carried out on chlorophyll fluorescence. The responses of fresh green and yellow senescent leaves and chlorophyll-decomposed chlorophyll mixtures in exhibiting fluorescence have been studied. The fluorescence signature is found to be a hyperspectral feature noticed as a small spike on the spectral reflectance curve of vegetation. The origin of the spike is justified and a quantitative estimation is made for the filling up of the absorption band depth. The possibility of presence or absence of the spike on the reflectance curve is explained. Also a technique is outlined for producing the oxygen absorption band around 760 nm artificially in laboratory.

4.2. Methodology

The experiment comprised leaf level and pigment level measurements. At leaf level, the reflectance from green and senescent leaf surfaces were measured throughout the ultraviolet-visible-near infrared (350-900 nm) region with 1 nm resolution with Analytical Spectral Devices (ASD) FieldSpec spectroradiometer having adjustable

angular field of view foreoptic arrangement. Angular field of view of 1 degree was maintained throughout so as to concentrate on a small zone. The reflectance values were normalized with respect to Spectralon white reference panel, generally accepted as practical Lambertian surface. Measurements were carried out under both solar illumination in open air and tungsten-halogen (TH) lamp illumination in laboratory.

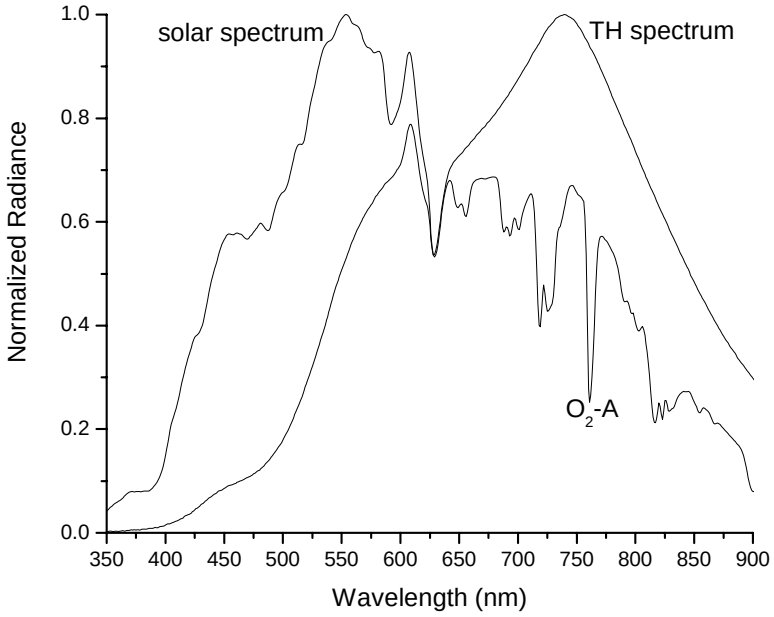

Figure 21: Normalized solar spectrum compared with normalized tungsten-halogen (TH) lamp spectrum. The solar spectrum exhibits the oxygen absorption band at around 760 nm.

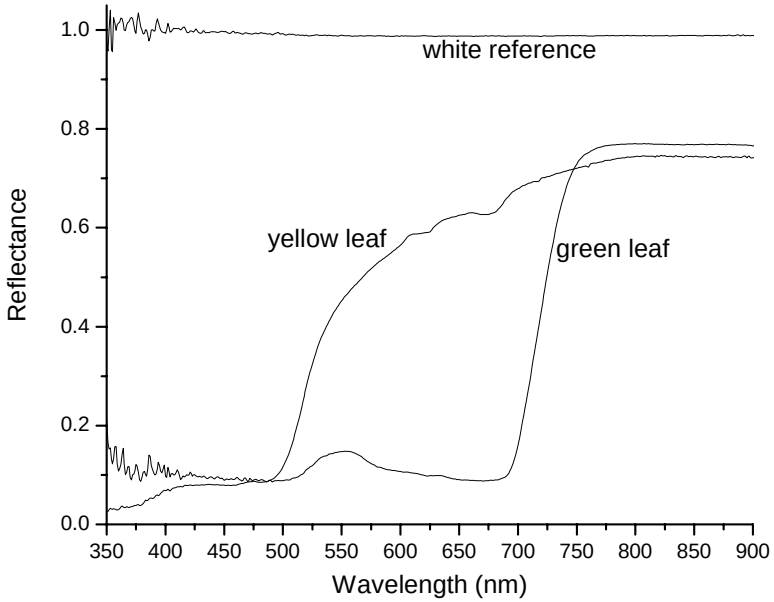

Figure 22: Reflectance-wavelength plots for pumpkin green and yellow leaf surfaces obtained under TH illumination. The reflectance of white reference surface, assumed to be unity, is also shown.

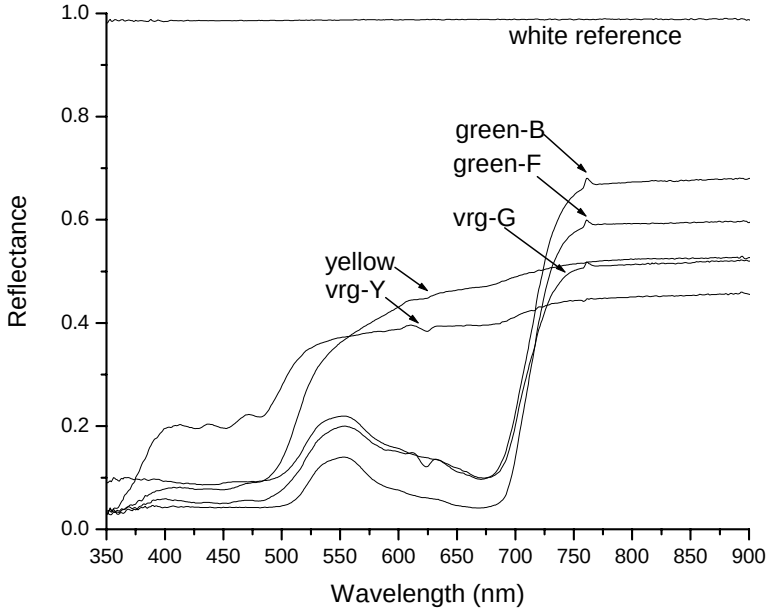

(a)

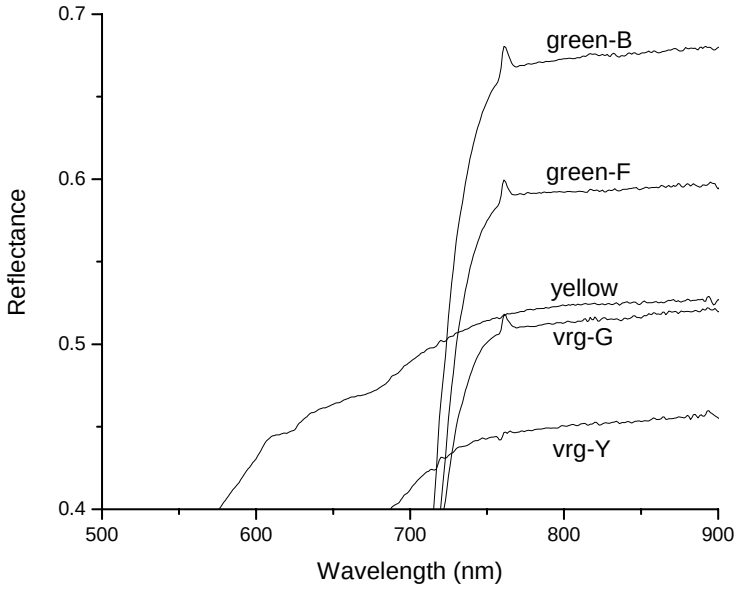

(b)

Figure 23: (a) Reflectance-wavelength plots obtained under solar illumination for front surface of pumpkin green leaf (green-F), back surface of pumpkin green leaf(green-B), green portion (vrg-G) and yellow portion (vrg-Y) of pothos variegated leaf and pumpkin senescent leaf (yellow), the symbols being indicated against the curves. The reflectance of white reference surface, assumed to be unity, is also shown. (b) Enlarged view of the curves around the fluorescence spikes at 760 nm.

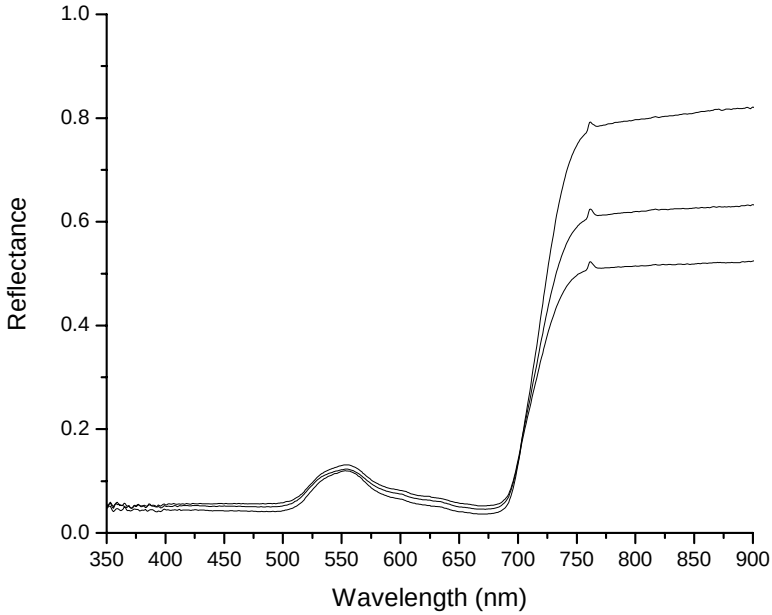

Figure 24: Reflectance-wavelength plots for three different leaves showing the maximum range of variation in reflectance and the persistence of fluorescence signature irrespective of that variation.

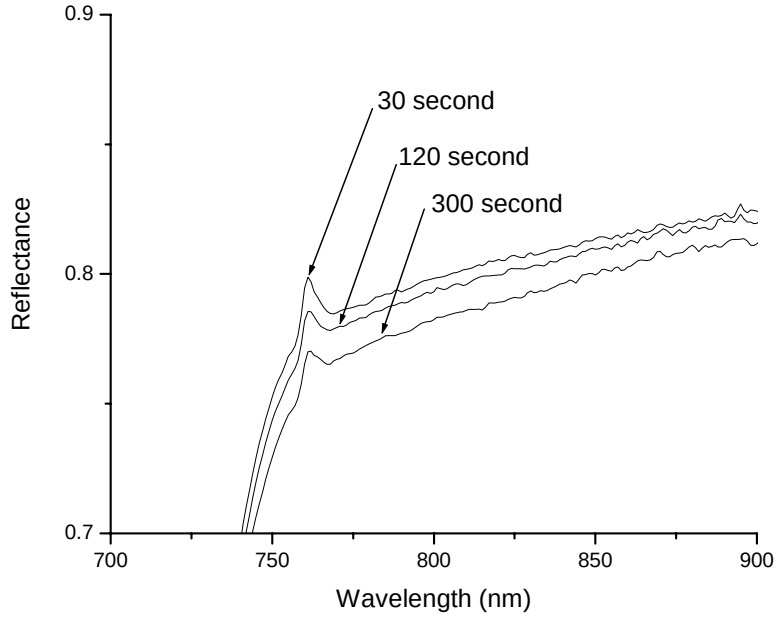

Figure 25: Reflectance-wavelength plots obtained at different times, indicated against the curves, after exposing to illumination from darkness.

Fresh and healthy leaves of pumpkin (*Cucurbita maxima*) at green (age of 7 days) and senescent yellow (age of 21 days) stages and yellow-green variegated leaves of pothos (*Epipremnum aureum*) were used for measurement. Reflectance was measured for both front and back sides of the pumpkin leaves and for the green and the pale yellow zones of the variegated leaves. To estimate the error in measurement, at least 10 leaves were measured in each case. To estimate the effect of steady-state fluorescence, the leaves were kept in darkness for 15 minutes and then the measurements were carried out immediately after exposing to illumination and also after keeping under illumination for 5 minutes. Measurement was repeated by keeping the leaf surface at different distances from the instrument. The results of the above leaf level measurements are presented in figures 21 to 26 and figures 29 (a) and (b).

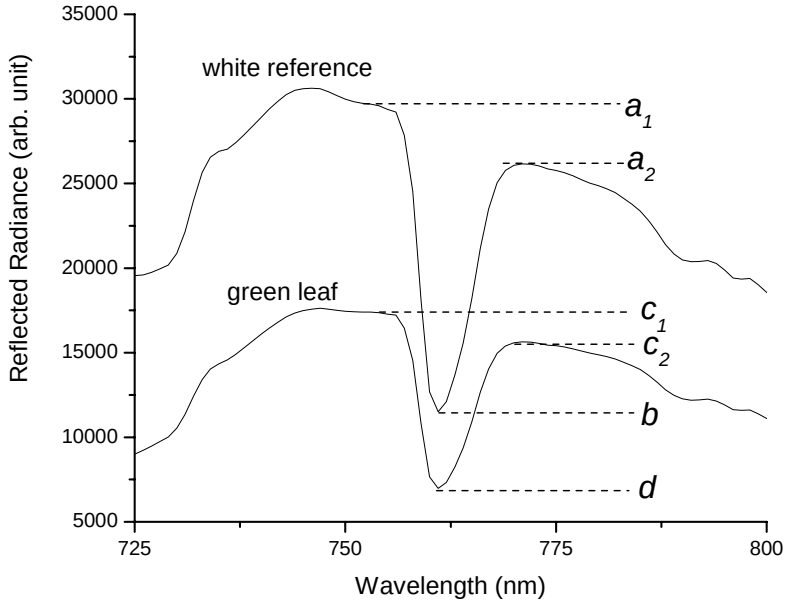

Figure 26: Estimation of fluorescence percentage from partial filling up of oxygen absorption band depth.

For pigment level study, two separate sample solutions were prepared in the following way. Fresh green and senescent pumpkin leaf crush, each of 5 g, were dipped separately in 200 ml of 80% acetone and preserved for 24 hours in darkness. Then the clear solution was centrifuged out. The solution with green leaf was expected to contain mixture of chlorophyll varieties and carotenoids and the solution with senescent leaf was expected to contain decomposed chlorophyll having lost the fluorescence capability. Sample solutions were prepared by mixing different volume ratios of the fresh and decomposed chlorophyll solutions.

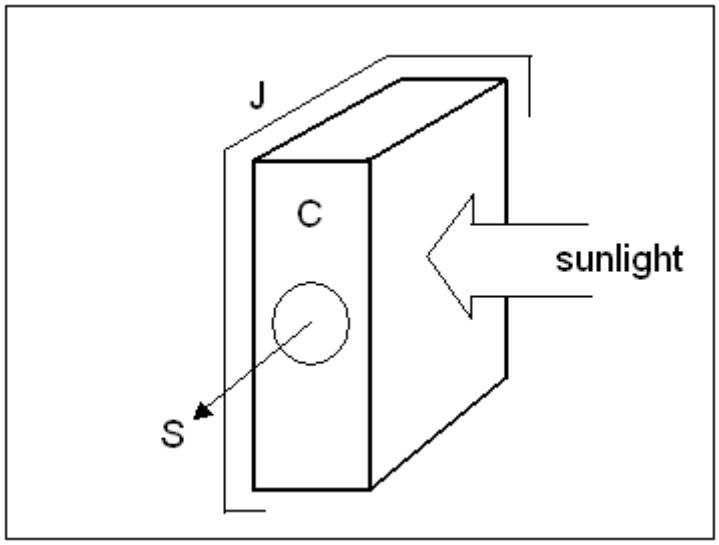

Figure 27: Experimental set up for detecting the fluorescence emission in chlorophyll solutions taken in cuvette (C) covered with black jacket (I) leaving one side open for incidence of sunlight. The spectroradiometer (S) is fitted perpendicularly to the opening on one end.

The arrangement sketched in Figure 27 was constructed to study the pigment level fluorescence with the same instrument as that for reflectance, namely the ASD spectroradiometer. The sample solutions were taken in glass cuvette (C) of 5 cm×5 cm side and 1cm thickness. The cuvette was covered from light with black jacket (J). Only one side was kept open to allow sunlight to be incident on the solution and a narrow opening on the end perpendicular to it was fitted with the 1 degree foreoptic of the spectroradiometer (S). It was expected to detect the mixture of diffused reflected sunlight and fluorescent emission. The results obtained with different proportions of fresh and decomposed chlorophyll solutions and the base solvent (80% acetone) are shown in figures 28 (a) and (b).

As a part of the experiment, the work investigated on the possibility of producing oxygen absorption band at 760 nm in laboratory. It outlined a prototype instrumental set-up for producing an artificial oxygen absorption band in laboratory to get the advantage of this absorption in absence of solar illumination. A glass tube of 50 cm length and 5 cm diameter with two flat ends and two openings with stoppers was employed, as shown in Figure 30. Sunlight was allowed to be incident through one end and the spectroradiometer foreoptic was fitted to the other end. Pumping out the air, pure oxygen gas was steadily blown through the openings. Thus the sunlight traversing through the

atmosphere was made to pass through an additional column of oxygen and air alternately. The changes in absorption depth in presence of oxygen and air in the tube are shown in Figure 31.

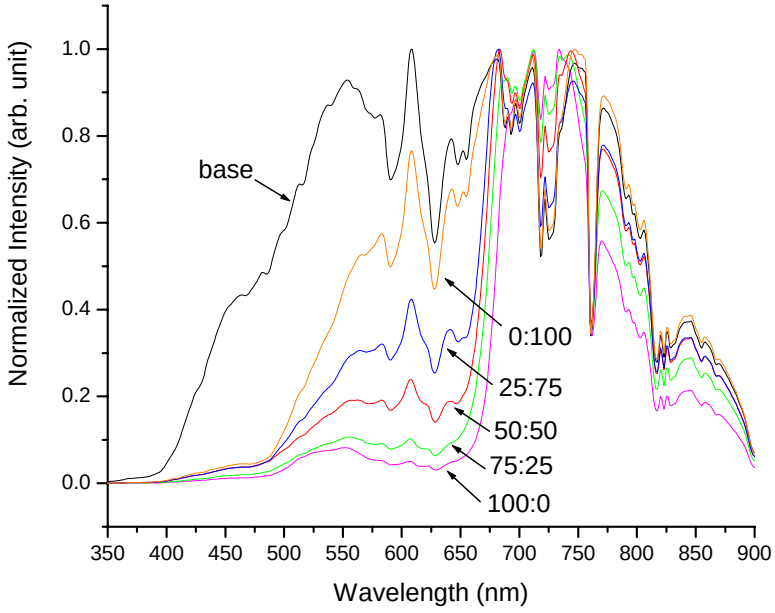

(a)

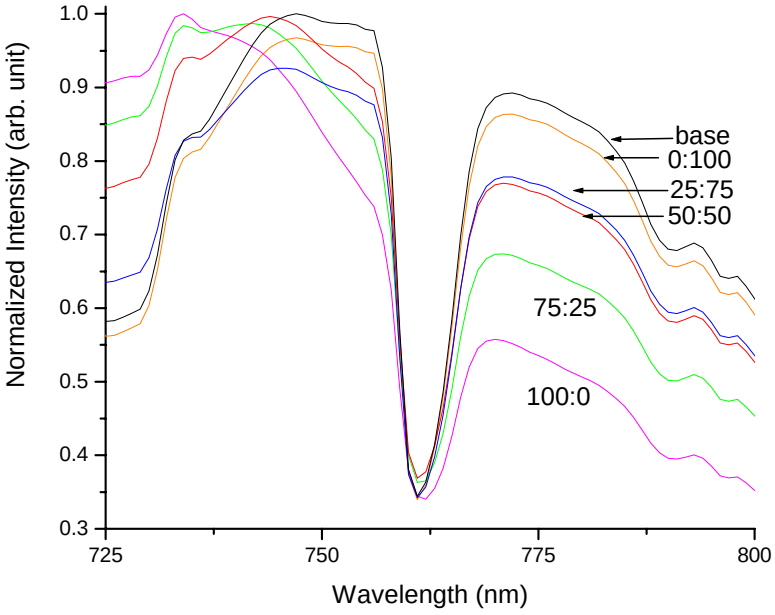

(b)

Figure 28: (a) Detected radiation intensities with the experimental set up of Fig. 4 with the solvent of 80% acetone (base) and solutions of different volume ratios of fresh and decomposed chlorophyll indicated

against the curves. (b) Enlarged view of the above showing the filling up of the absorption band around 760 nm.

4.3. Results and Discussion

Figure 21 shows the radiance spectra for solar and TH illuminations. The radiance values are normalized to bring within the same scale for comparison. The nature of the TH lamp spectrum is not exactly similar to the solar spectrum. The violet and blue regions, the major contributors to chlorophyll fluorescence are weaker in TH spectrum, as shown in the figure. The main difference in the present context is that the solar spectrum consists of a sharp, deep groove at around 760 nm due to oxygen absorption because the solar radiation reaches the earth after passing through the whole atmospheric column. This absorption feature is absent in the TH spectrum produced in laboratory.

Figure 22 represents the reflectance-wavelength plots for green and yellow leaf surfaces obtained under TH illumination. Figure 23 represents the reflectance-wavelength plots for different leaves under solar illumination.

Comparing Figure 22 with Figure 23(a) it is noted that the overall reflectance characteristics for green and senescent (yellow) leaves exhibit similar nature under outdoor solar illumination and indoor TH lamp illumination. But a marked difference is the presence of a small spike on the reflectance curve at 760 nm under solar illumination. The enlarged view of Figure 23 (b) clarifies this feature. The spike is obtained with both the front (green-F) and back (green-B) surfaces of green leaf. It is present with the reflectance of the green portion (vrg-G) of the variegated leaf also. But the spike is not present without chlorophyll, as in the naturally senescent (yellow) leaf and the yellow portion (vrg-Y) of the variegated leaf. Obviously the spike is the signature of chlorophyll. It originates from the partial filling up of the O_2–A absorption depth due to fluorescence emission of chlorophyll.

To estimate the error in measurement, reflectance spectra were procured for different leaves at similar conditions. Some examples are shown in Figure 24. It is noted that the reflectance value widely varies, but the nature of variation remains the same and the fluorescence signature persists irrespective of the amount of reflectance.

To estimate the characteristic of steady-state fluorescence, the leaves were kept in darkness for 15 minutes and then the reflectance-wavelength measurements were carried

out immediately after exposing the leaf to illumination and also after keeping it under illumination up to 5 minutes.

Figure 25 shows some such examples with large magnification of the reflectance curve around the fluorescence. The time of light exposure after darkness is indicated against the curve. Some difference in fluorescence spike height is noted with the time of measurement after exposure from dark condition. However, in normal scale, as in the other figures, this difference is indistinguishable. Hence, fluorescence under steady illumination is reported throughout. All of the previous works on vegetation reflectance did not report such fluorescence signature in vegetation reflectance curve. Wang *et al*. [22] observed it but totally ignored. Zarco-Tejada *et al*. [12] identified it as a result of fluorescence and attempted to explain with software simulation.

Figure 26 suggests a quantification of the extent of fluorescence. It represents the enlarged view of the reflected radiance spectral variation around O_2–A band from the white reference surface and that from the green leaf surface. It is obvious that the fluorescence emission partially fills up the O_2–A absorption depth. When the ratio of these two radiance values is calculated for reflectance determination, an excess value is obtained that appears as a spike-like shape on the reflectance curve.

To quantify the filling up of the absorption well, the previous formulation [14, 17] is slightly modified, as follows. Since the baseline outside the absorption well is tilted in Figure 26, the average radiance outside the absorption well of white reference surface is

$$a = (a_1 + a_2)/2 \tag{5}$$

and that outside the absorption well of target (green leaf) is

$$c = (c_1 + c_2)/2 \tag{6}$$

The corresponding residual radiance at the bottom of the well are b and d, respectively. The reflectance coefficient is defined as

$$R = (c - d)/(a - b) \tag{7}$$

The two extreme limits of R are 1 and 0, respectively.

(i) When no filling up occurs due to fluorescence, $(c - d) = (a - b)$ and $R = 1$.

(ii) When the whole of the well is filled up due to fluorescence (though impossible), $(c - d) = 0$ and $R = 0$.

Thus the fluorescence percentage (f) can be defined in terms of R and absorption depths as

$$f = [(d - Rb)/c] \times 100\% \quad (8)$$

(i) When $R = 1$, the absorption depths for white reference and target are equal and $b = d$ so that $f = 0\%$.

(ii) When $R = 0$ (a hypothetical case), absorption depth is zero and $c = d$ so that $f = 100\%$.

Table-3: Fluorescence percentage (f) for reflectance in Figure 26 and different conditions of emission in Figure 28(b)

Calculation Parameter	f (%)
Reflectance in Figure 26	0.38
Emission in Figure 28(b) for different ratios of chlorophyll/decomposed chlorophyll as mentioned below:	
0:100	2.61
25:75	8.15
50:50	12.28
25:75	17.60
100:0	24.21

The value of f obtained from Figure 26 is listed in Table-3. Similar results of absorption depth filling were obtained with chlorophyll solutions of different volume ratios, as shown in Figure 28(b). The fluorescence emission increases and fills up larger portion of the depth on increasing the chlorophyll content. Following a similar process as above, the f values for different volume ratios of chlorophyll were calculated from Figure 28(b) and compiled in Table-3. The present values, though obtained with arbitrary concentrations, can demonstrate the enhancing of fluorescence emission with the increase of chlorophyll content. Comparing the fluorescence in reflection from leaf surface with

that in extracted chlorophyll solution it is noted that the former is very feeble. It is expected because the fluorescence in reflection [figures 21 to 25] was detected with respect to full sun whereas the fluorescence in extracted solution [figures 28(a) and (b)] was detected with respect to only a fraction of the sunlight diffused through the solution.

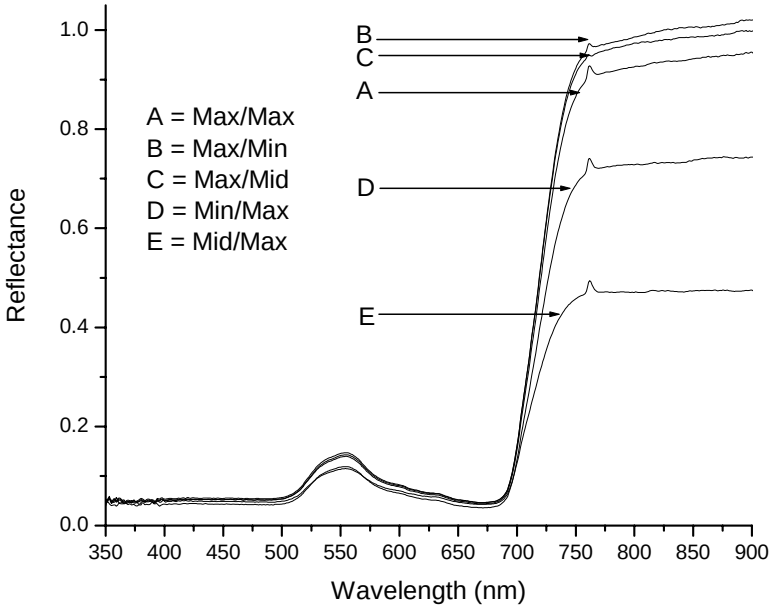

(a)

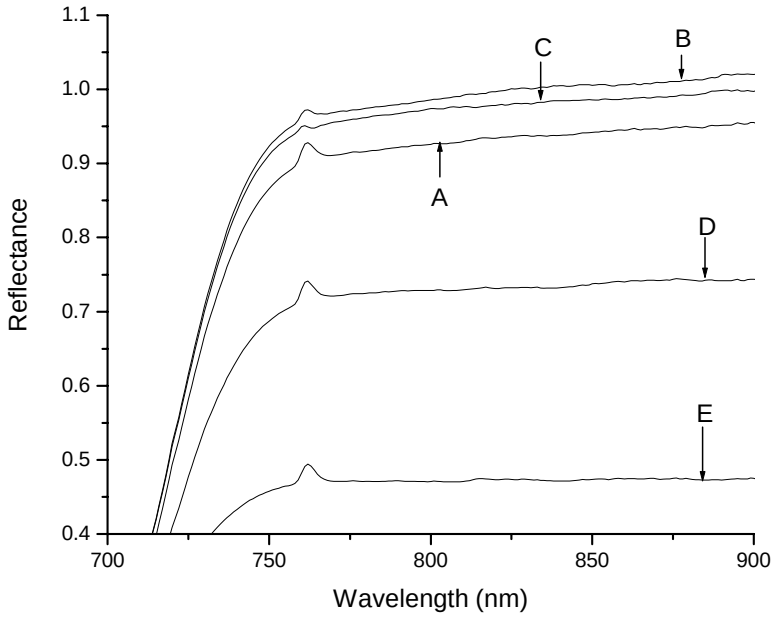

(b)

Figure 29: (a) Demonstration of existence or non-existence of fluorescence spike in spectral reflectance curve with correct (Curve-A) and incorrect (Curves B, C, D and E) ratios of three different radiation intensities, namely Min, Mid and Max for leaf surface and corresponding white surface. (b) The enlarged view of the above around fluorescence wavelengths.

The question arises then, why did not all of the previous researchers obtain such spike-like fluorescence signature in vegetation reflectance? The reason is the fluctuation in calibration with respect to white reference panel. The reflectance is the ratio of the reflected radiance from vegetation surface to that from white reference surface. The leaf radiance correctly calibrated with the corresponding white radiance yields the proper fluorescence spike. Wrong calibration with other white radiance values either underestimates or overestimates the reflectance. Thus the spike may either disappear or get more pronounced. To simulate such possible error, three different reflectance values of the same green leaf surface measured at distance of 15 cm, 25 cm and 35 cm, respectively were considered. Each one was individually calibrated with respect to white surface. The intensities of reflected radiance were obviously different due to the combined effect of the change in distance and the area under the field of view. Thus three different values of the reflected radiance intensity were obtained, hence named ‘Min’,

'Max' and 'Mid', respectively. It is apparent from Figure 29(a) and its enlarged view [Figure 29(b)] that the leaf radiance calibrated with the correct corresponding white radiance yields the proper fluorescence spike, as in Curve-A. But wrong calibration with other white radiance either underestimates the spike, as in Curve-B and Curve-C or overestimates it, as in Curve-D and Curve-E. Thus the spike may either disappear or get more pronounced. The probability of disappearing is higher because the solar illumination generally increases up to solar noon and white calibration may not be performed at every moment. If the white calibration remains fixed at lower value, absence of fluorescence spike occurs similar to curves B and C.

The interesting feature in the above discussion is that except for the distortion of the fluorescence spike at around 760 nm, the usual nature of reflectance variation with wavelength remains the same at different calibrations. Thus, to observe the fluorescence signature properly in the vegetation reflection spectra, the solar illumination must be constant, which is not possible always. The reference level may fluctuate due to passing cloud or other atmospheric phenomena. Such limitation of solar illumination may be overcome with the use of artificial illumination like TH lamp that can be suitably controlled and maintained at fixed intensity. But that does not contain the oxygen absorption band because the light does not pass through several kilometers of oxygen column like the solar illumination. The usefulness of this band is highlighted in the introduction.

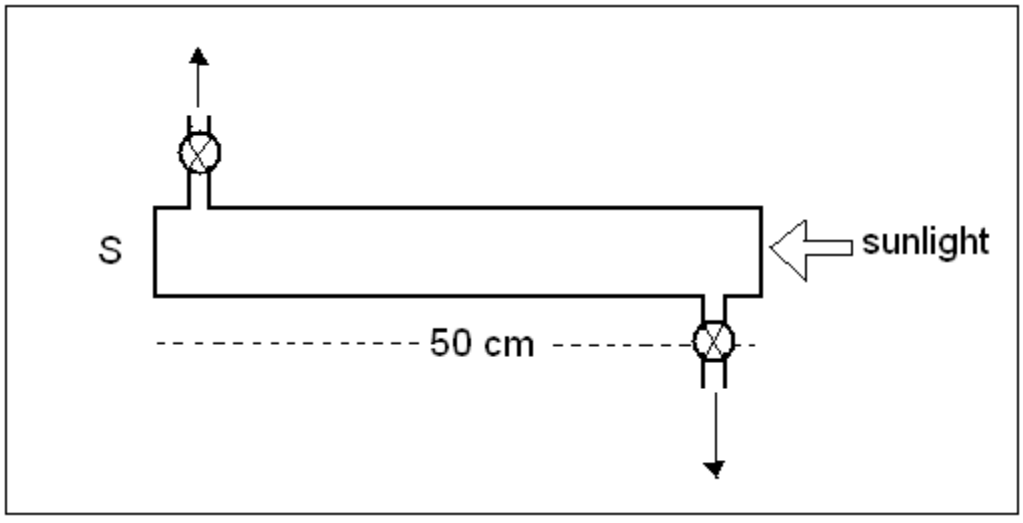

Figure 30: Experimental set up for studying the change in oxygen absorption depth with the use of oxygen column of 50 cm length. The sunlight is allowed from one end and the spectroradiometer (S) is fitted to the other end.

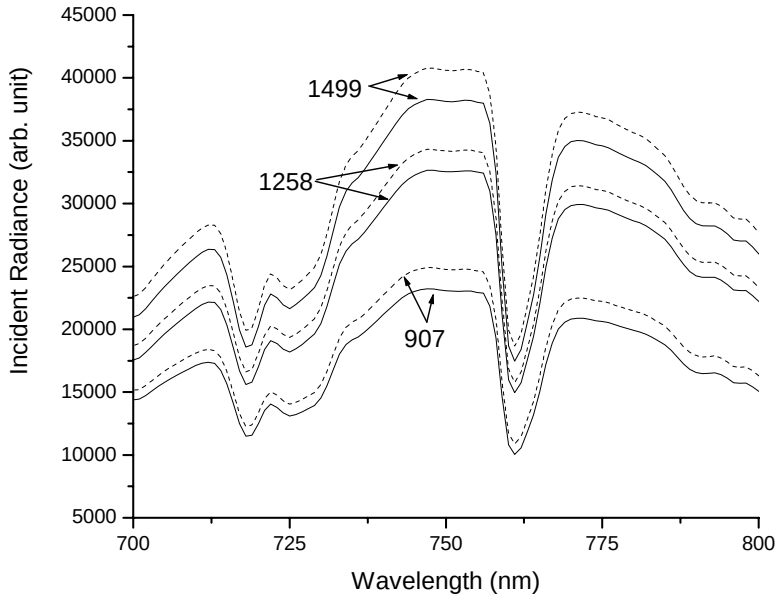

Figure 31: The increase (shown with dotted lines) of oxygen absorption depth in presence of the 50 cm oxygen column at different solar radiation intensities ($\mu mol.m^2.s^{-1}$) indicated against the curves.

The next point of discussion originating from the above fact is the possibility of observing oxygen absorption of radiation at 760 nm in laboratory. That is possible either by using an oxygen column of abnormal length, comparable to atmospheric height or by compressing the oxygen to high density. The later one is, of course, the practically achievable method. Following Lambert-Beer law, the radiation intensity transmitted through the gas should exponentially increase with gas concentration for a fixed length of gas column. Assuming the pressure to be proportional to gas concentration, increase in absorption depth from 10% to 99.9% would call for a pressure rise of the order of 2300 times. The construction of a robust apparatus for this purpose is an engineering job of high technical perfection. The present work could not carry out the whole job but outlined the significance of such an instrumental set-up, as indicated in Figure 30 mentioned earlier. The results are shown in Figure 31 and Table-4. It is noted that solar radiation, when passes through an additional column of oxygen at atmospheric pressure,

undergoes about 10% increase in absorption depth irrespective of illumination intensity. The results assure the possibility of generating oxygen absorption depth in spectral curve, similar to that in atmosphere, with artificial illumination in laboratory to facilitate the observation of vegetation reflectance through oxygen absorption band in laboratory.

Table-4: Increase in oxygen absorption band depth due to the presence of 50 cm oxygen column at different solar illumination intensities

Solar illumination intensity ($\mu mol.m^2.s^{-1}$)	Increase in absorption band depth (%)
1499	11.5
1258	9.5
907	7.3

4.4. Conclusion

Investigations were carried out on the hyperspectral signature of solar induced fluorescence found in the reflection spectrum of vegetation at the oxygen absorption band around 760 nm. The signature was detected as a small spike-like variation on the spectral reflectance curve. The origin was justified with both leaf level and pigment level measurements with ASD spectroradiometer. Leaf reflectance was measured for both front and back side of the leaf and for the green and the pale yellow zones of variegated leaves. The change in fluorescence with time elapsed after exposure from darkness was studied. The pigment-level measurements were carried out with different volume ratios of fresh and decomposed chlorophyll in solution. The extent of fluorescence was quantified in terms of the filling up of the oxygen absorption well. It was demonstrated that the small spike could be lost or misinterpreted due to small fluctuation in the reference level of calibration for reflectance. To observe the peak, the solar illumination must be constant. Also a technique was outlined for constructing an oxygen radiation absorption simulator in laboratory.

REFERENCES

1. J. Fischer and H. Grasl, “Detection of cloud-top height from backscattered radiances within the oxygen A band. Part 1: Theoretical study”, *J. Appl. Meteorology*, vol. 30, pp. 1245-1259, 1991.

2. R.B.A. Koelemeijer, P. Stammes, J.W. Hovenier and J.F. de Haan, “A fast method for retrieval of cloud parameters using oxygen A band measurements from the Global Ozone Monitoring Experiment”, *J. Geophys. Res*., vol. 106, pp. 3475-3490, 2001.

3. N. Fournier, P. Stammes, M. de Graaf, R. van der A, A. Piters, M. Grzegorski and A. Kokhanovsky, “Improving cloud information over deserts from SCIAMACHY Oxygen A-band measurements”, *Atmos. Chem. Phys.*, vol. 6, pp. 163–172, 2006.

4. P. Kiedron, J. Berndt, J. Michalsky, and L. Harrison, “Column water vapor from diffuse irradiance”, *Geophys. Res. Lett*., vol. 30, pp. 1565-1568, 2003.

5. P. Dubuisson, R. Borde, C. Schmechtig and R. Santer, “Surface pressure estimates from satellite data in the oxygen A-band: Applications to the MOS sensor over land”, *J. Geophys. Res*., vol. 106, pp. 27277-27286, 2001.

6. D. Ramon, L. Cazier, and R. Santer, “The surface pressure retrieval in the MERIS O_2 absorption: validation and potential improvements”, *IEEE Int. Geosc. Remote Sens. Symposium IGARSS’2003*, vol. 5, pp. 3126-28, 2003.

7. Govindjee, “Sixty-three years since Kautsky: Chlorophyll a fluorescence” *Aust. J. Plant Physiol.*, vol. 22, pp. 131-160, 1995.

8. Govindjee, “Chlorophyll a fluorescence: a bit of basics and history” in *Chlorophyll a Fluorescence: A Signature of Photosynthesis: Advances in*

Photosynthesis and Respiration, vol. 19, pp. 1-42, G.C. Papageorgiou and Govindjee, Eds., Springer, Dordrecht, 2004.

9. K. Maxwell and G.N. Johnson, "Chlorophyll fluorescence – a practical guide", *J. Expt. Bot.*, vol. 51, pp. 659-668, 2000.

10. A.A. Gitelson, C. Buschmann and H.K. Lichtenthaler, "The chlorophyll fluorescence ratio *F*735/*F*700 as an accurate measure of the chlorophyll content in plants", *Remote Sens. Environ*., vol. 69, pp. 296-302, 1999.

11. M. Meroni, M. Rossini, V. Picchi, C. Panigada, S. Cogliati, C. Nali and R. Colombo, "Assessing steady-state fluorescence and PRI from hyperspectral proximal sensing as early indicators of plant stress: The case of ozone exposure", *Sensors*, vol. 8, pp. 1740-1754, 2008.

12. P.J. Zarco-Tejada, J.A.J. Berni, L. Suarez, G. Sepulcre-Canto, F. Morales and J.R. Miller, "Imaging chlorophyll fluorescence with an airborne narrow-band multispectral camera for vegetation stress detection", *Remote Sens. Environ*., vol. 113, pp. 1262-1275, 2009.

13. I. Moya, M. Silvestri, O. Vallon II, G. Sinque and R. Bassi, "Time-resolved fluorescence analysis of the photosystem II antenna proteins in detergent micelles and liposomes", *Biochemistry*, vol. 40, pp. 12552-12561, 2001.

14. (a) I. Moya, L. Camenen, S. Evain, Y. Goulas, Z. G. Cerovic, G. Latouche, J. Flexas and A. Ounis, "A new instrument for passive remote sensing: 1. Measurements of sunlight-induced chlorophyll fluorescence", *Remote Sens. Environ*., vol 91, pp. 186-197, 2004.
(b) I. Moya and Z. G. Cerovic, "Remote sensing of chlorophyll fluorescence: instrumentation and analysis", in *Chlorophyll a Fluorescence: A Signature of*

Photosynthesis: Advances in Photosynthesis and Respiration, vol. 19, pp 429-445, G.C. Papageorgiou and Govindjee, Eds., Springer, Dordrecht, 2004.

15. P.J. Zarco-Tejada, J.R. Miller and G.H. Mohammed, "Remote sensing of solar-induced chlorophyll fluorescence from vegetation hyperspectral reflectance and radiative transfer simulation" in *From Laboratory Spectroscopy to Remotely Sensed Spectra of Terrestrial Ecosystems*, pp. 233-269, R. S. Muttiah, Ed., Kluwer Academic, Dordrecht, 2002.

16. M. Ostrowska, R. Majchrowski, D.N. Matorin and B. Wozniak, "Variability of the specific fluorescence of chlorophyll in the ocean. Part I. Theory of classical in situ chlorophyll fluorometry, *Oceanologia*, vol. 42, pp. 203-219, 2000.

17. A.F. Theisen, "Detecting chlorophyll fluorescence from orbit" in *From Laboratory Spectroscopy to Remotely Sensed Spectra of Terrestrial Ecosystems*, pp. 203-232, R. S. Muttiah, Ed., Kluwer Academic, Dordrecht, 2002.

18. J. Grace, C. Nichol, M. Disney, P. Lewis, T. Quaife and P. Bowyer, "Can we measure terrestrial photosynthesis from space directly, using spectral reflectance and fluorescence?" *Global Change Biol*., vol. 13, pp. 1484-1497, 2007.

19. Z. Malenovsky, K.B. Mishra, F. Zemek, U. Rascher and L. Nedbal, "Scientific and technical challenges in remote sensing of plant canopy reflectance and fluorescence", *J. Expt. Bot.*, vol 60, pp. 2987-3004, 2009.

20. L. Liu; Y. Zhang; J. Wang and C. Zhao, "Detecting solar-induced chlorophyll fluorescence from field radiance spectra based on the Fraunhofer line principle", *IEEE Trans. Geosci. Remote Sensing*, vol. 43, pp. 827-832, 2005.

21. M. Meroni and R. Colombo, “Leaf level detection of solar induced chlorophyll fluorescence by means of a subnanometer resolution spectroradiometer”, *Remote Sens. Environ.*, vol. 103, pp. 438-448, 2006.

22. Y. Wang, W. Buermann, P. Stenberg, H. Smolander, T. Hame, Y. Tian, J. Hu, Y. Knyazikhin, and R. B. Myneni, “A new parameterization of canopy spectral response to incident solar radiation: case study with hyperspectral data from pine dominant forest”, *Remote Sens. Environ*, vol. 85, pp. 304-315, 2003.